

Lead-free Organic–Inorganic Hybrid Perovskites for Photovoltaic Applications: Recent Advances and Perspectives

Zejiào Shi, Jià Guo, Yonghua Chen,* Qi Li, Yufeng Pan, Haijuan Zhang, Yingdong Xia,* and Wei Huang*

Organic–inorganic hybrid halide perovskites (e.g., MAPbI₃) have recently emerged as novel active materials for photovoltaic applications with power conversion efficiency over 22%. Conventional perovskite solar cells (PSCs); however, suffer the issue that lead is toxic to the environment and organisms for a long time and is hard to excrete from the body. Therefore, it is imperative to find environmentally-friendly metal ions to replace lead for the further development of PSCs. Previous work has demonstrated that Sn, Ge, Cu, Bi, and Sb ions could be used as alternative ions in perovskite configurations to form a new environmentally-friendly lead-free perovskite structure. Here, we review recent progress on lead-free PSCs in terms of the theoretical insight and experimental explorations of the crystal structure of lead-free perovskite, thin film deposition, and device performance. We also discuss the importance of obtaining further understanding of the fundamental properties of lead-free hybrid perovskites, especially those related to photophysics.

1. Introduction

Organic–inorganic hybrid halide perovskite solar cells (PSCs) have in the past few years attracted intense attention and risen as one of the most promising solar cells with power conversion efficiency (PCE) over 22%.^[1–22] Along with the advantages of cost-effective solution-processability, PSC fabrication is now comparable to state-of-the-art commercial photovoltaic

Z. Shi, J. Guo, Prof. Y. Chen, Y. Pan, H. Zhang,
Prof. Y. D. Xia, Prof. W. Huang
Key Laboratory of Flexible Electronics (KLOFE) &
Institute of Advanced Materials (IAM)
Jiangsu National Synergistic Innovation Center
for Advanced Materials (SICAM)
Nanjing Tech University (NanjingTech)
30 South Puzhu Road, Nanjing 211816, P. R. China
E-mail: iamyhchen@njtech.edu.cn;
iamydxia@njtech.edu.cn; wei-huang@njtech.edu.cn



Dr. Q. Li
Physical Sciences Division
IBM TJ Watson Research Center
Yorktown Heights, NY 10598, USA

Dr. Q. Li
Department of Computer Science
University of Illinois at Urbana-Champaign
Urbana, IL 61801, USA

DOI: 10.1002/adma.201605005

techniques including silicon, CdTe, CuIn-GaSe, and GaAs, fulfilling the requirements for the large-scale deployment of solar energy. This is the first time that such a novel solar cell has been able to compete with commercially available devices so successfully. Most importantly, there is no sign that the PCE of PSCs will face an insurmountable bottleneck.

As the core unit to realize high performance, organic–inorganic hybrid perovskite materials have a structure of ABX₃ (A: CH₃NH₃⁺, CH(NH₂)₂⁺, Cs⁺, B: Pb²⁺, Sn²⁺; X: Cl⁻, Br⁻ or I⁻),^[23–44] where the A cation resides at the eight corners of the cubic unit while the B cation is located at the center of the body of an octahedral [BX₆]⁴⁻ cluster.^[45] In the typical ABX₃ structure, A, B, and X ions must correspond to the tolerance factor $t = (R_A + R_B) / [\sqrt{2}(R_X + R_B)]$

where R_A , R_B , and R_X are the ionic radii for the A, B, and X position, respectively. The ideal t should be 1 which can wave between 0.813 and 1.107,^[23] otherwise the cubic or cubic-like crystal structure will be tortured, warped, and finally destroyed. There are a variety of organic–inorganic hybrid halide perovskites, corresponding to the tolerance factor t .^[23] In most common lead halide perovskites, the A position represents an organic or metal cation, e.g., methylammonium (MA⁺), formamidinium (FA⁺), and Cs⁺, which should be large enough to meet the tolerance factor t due to the large radius of Pb²⁺ in the B position, while the C positions are halogen anions or their mixtures, which forms the 3D perovskite structure.^[46] The crystal structure provides the fantastic properties of perovskite materials, such as long carrier recombination lifetime, wide absorption of light, long exciton diffusion length, high charge mobility, which has led perovskites to be popular in photovoltaic applications.^[46–58]

Despite the intensive development of PSCs, because of the attracted attention of an unprecedented number of solar cell researchers, Pb²⁺ is still necessary to achieve high performance. Unfortunately, the toxicity issue of lead has led to a bottleneck to further development. The maximum Pb²⁺ content was set at the level of 0.15 μg L⁻¹ and 15 μg L⁻¹ in air and water, respectively, by the U.S. EPA.^[59] Pb²⁺ in PbI₂, which is the product of the decomposition of perovskites, has a larger solubility (K_{sp}) on the order of 1×10^{-8} than the K_{sp} on the order of $\approx 1 \times 10^{-22}$

of conventionally toxic Cd^{2+} in CdTe ,^[60] which has been processed with recycling progress in past years due to its toxicity. This indicates a higher toxic level of Pb^{2+} than Cd^{2+} in their corresponding solar cells materials. Toxicity, long degradation lifetime, and stability in the ecosystem determine that once the lead and its compounds pollute the soil or water, the harm to the earth and human beings is almost eternal. The facts also imply that the pollution of lead in our living earth will be hard to control if mass production of conventional MAPbI_3 PSCs are realized.^[61] Regardless of the high performance of lead-based PSCs, therefore, it is obligatory to pave a new path to explore environmentally-friendly lead-free perovskite materials for photovoltaic applications.

In this review, we primarily highlight organic–inorganic hybrid environmentally-friendly perovskite materials and their related solar cell applications. Specifically, we summarize the previous works on lead-free PSCs in terms of theoretical calculations and experimental studies. From the view point of theoretical calculations, we investigate theoretical calculation methods developed in recent years to make it clear what similarities and differences exist between lead-based PSCs and lead-free PSCs. Then we proceed to discuss the structure and optoelectronic properties of lead-free PSCs, and how to make the non-toxic lead-free PSCs superior by theoretical calculation. Most importantly, we give more attention to experimental insights including the precursor preparation, device fabrication and the characterization of optoelectronic properties for lead-free PSCs. The different metal ions are systematically addressed, including IV A group ions, e.g., Sn^{2+} and Ge^{2+} , V A group ions with similar isoelectronic structure, e.g., Bi^{3+} and Sb^{3+} , and other ions, as shown in **Figure 1**. It is shown that replacing Pb^{2+} with the alternative metal ions with not much change in the crystal structure and optoelectronic properties in PSCs has not yet been demonstrated but could be reached through further advances in material processing. Finally, we give an outlook on both achievements and challenges remaining on lead-free PSCs. We think great effort is needed to explore high-performance lead-free PSCs in further understanding the fundamentals of lead-free perovskites.

2. Theoretical Calculations of Lead-free Organic–Inorganic Hybrid Perovskites

First principles calculation based on density functional theory (DFT)^[62,63] is a modelling method to simulate the electronic structures of many body systems from atomic level quantum mechanics. Recently, first principles calculations have been utilized as an important tool for investigating lead-free perovskites as replacements for MAPbI_3 . Electronic structures of various lead-free perovskites were calculated to simulate their electron/hole effective masses, band gaps, carrier mobilities, theoretical absorption spectra, and other properties related to their potential solar cell applications. It is worth emphasizing that the choice of exchange–correlation functions used in DFT calculations is not unique. In fact, the exchange–correlation functional is the sole unknown and approximation in the whole theory; nevertheless, it is so important that the selection might affect the results of the DFT calculations qualitatively. Traditionally,



Zejiao Shi received a BE Degree in Inorganic Nonmetallic Material Engineering from Nanjing Tech University in 2014. He is currently a PhD candidate in the Institute of Advanced Materials (IAM), Nanjing Tech University under the supervision of Prof. Yonghua Chen. His research interest is lead-free organic–inorganic hybrid perovskite solar cells.



Yonghua Chen received a BE in Chemistry from Inner Mongolia University in 2006 and a PhD degree in Polymer Chemistry and Physics at the Changchun Institute of Applied Chemistry, Chinese Academy of Sciences, in 2011. Afterward, he spent time at Wake Forest University (2 years) and Case Western Reserve University (2 years) as a postdoctoral researcher.

He is currently a full professor at Nanjing Tech University. His research interests are organic and organic/inorganic hybrid optoelectronic materials and devices for flat panel displays and solid state lighting, and for energy conversion.



Wei Huang received his BSc, MSc, and PhD degrees in Chemistry from Peking University in 1983, 1988, and 1992, respectively. In 2001, he became a chair professor at Fudan University, where he founded the Institute of Advanced Materials. In June 2006, he was appointed the Deputy President of Nanjing University of Posts and

Telecommunications, where he founded the Key Laboratory for Organic Electronics and Information Displays. In July 2012, he was appointed the President of Nanjing Tech University. He is a member of the Chinese Academy of Sciences. His research interests include organic optoelectronics, nanomaterials, flexible electronics, and bioelectronics.

the local density approximation (LDA) and the generalized gradient approximation (GGA) functionals have had great success in many systems, despite their relative simplicity. However,

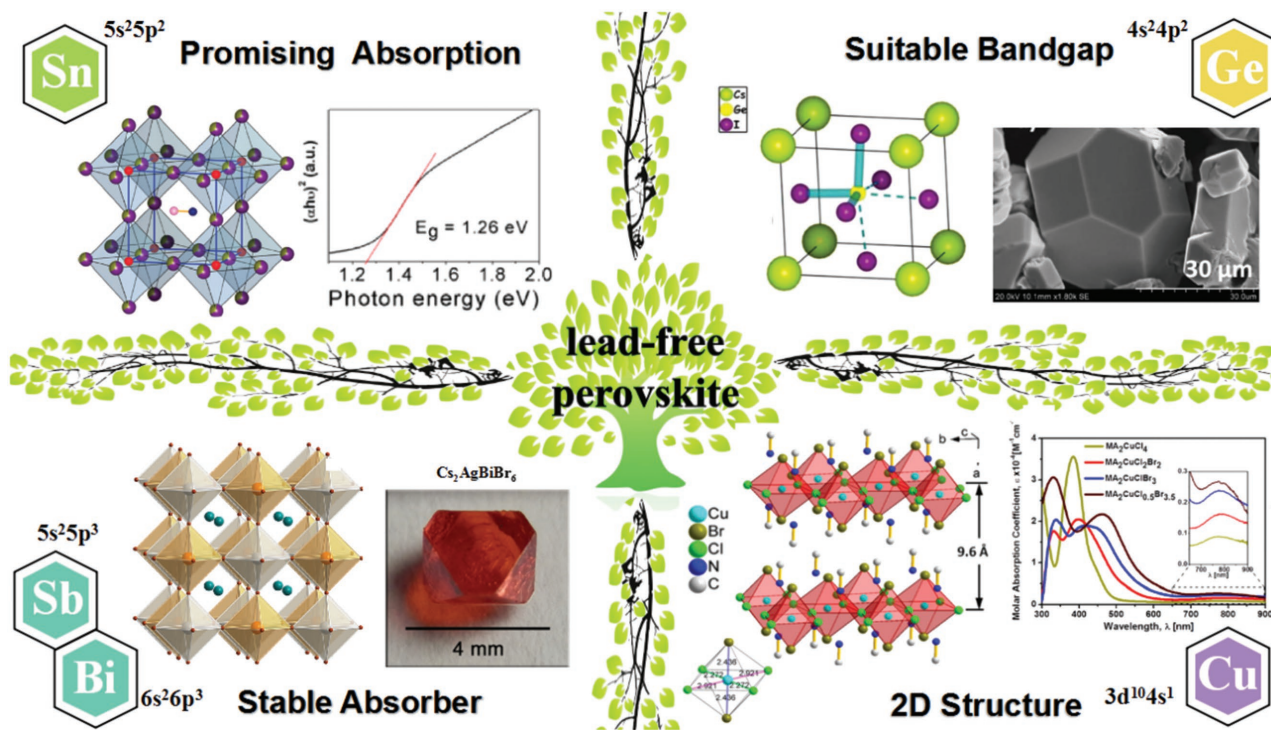


Figure 1. Promising metal ions for lead-free organic–inorganic hybrid perovskites. The image of Sn-based perovskite solar cells is reproduced with permission.^[68] Copyright 2014, Macmillan Publishing. The image of Ge-based perovskite solar cells is reproduced with permission.^[123] Copyright 2015, American Chemical Society. The image of Bi and Sb-based perovskite solar cells is reproduced with permission.^[152] Copyright 2016, American Chemical Society. The image of Cu-based perovskite solar cells is reproduced with permission.^[158] Copyright 2016, American Chemical Society.

LDA and GGA exhibit serendipitous cancellations between their exchange and correlation parts, which leads to unphysical electron self-interactions. As a result, the local (LDA) and semi-local (GGA) functions intrinsically underestimate band gaps of solids by 30–100%.^[64] To overcome this fundamental problem, methods/functions including the GW approximation,^[65] time-dependent DFT (TDDFT),^[66] HSE03, HSE06, and PBE0 hybrid functionals,^[67–71] and more recent Delta self-consistent-field method^[72] have been developed and applied to recent theoretical calculations on lead-free perovskites. Spin-orbit coupling (SOC) is required to be included in calculations with the presence of heavy atoms to achieve a more accurate prediction of electronic structures. Long range van der Waals interactions are optionally included in recent calculations on lead-free perovskites under different schemes including the DFT-D approach,^[73] the DFT-D2 method of Grimme,^[74] and the vdW-DF functional of Langreth et al.^[75]

For a perovskite ABX_3 , the octahedral factor and tolerance factor are commonly used as criteria to determine if it can crystallize in the perovskite structure, where r_A , r_B , and r_X are the ionic radii of atom A, B, and X, respectively. Empirical observations suggest that an ABX_3 compound is likely to form in a perovskite structure with a tolerance factor between 0.7 and 1.1.^[76] However, accurate ionic radii data are not entirely transferable to different compounds, and there are limitations on the predictions of the empirical criteria. Filip et al. used randomly displaced structures (atom positions and lattice parameters) to investigate the stability of possible lead-free perovskites.^[77] Making the stability and desired calculated band gap as two

concurrent conditions, they identified 25 compounds out of 248 candidates for possible solar cell applications with high-throughput screening, as shown in **Figure 2**. As a promising candidate, $AMgI_3$ exhibited exceptionally dispersive conduction bands (hence low electron effective mass), and tunable band gap between 0.9 to 1.7 eV by varying A^+ ion size. Partial substitution of Pb by Mg was suggested as a promising route to reduce the toxicity of organic–inorganic metal–halide perovskites without losing solar cell efficiency substantially.

Sun et al. investigated a potential replacement of Pb^{2+} with Ge^{2+} with GGA and vdW-D2 functional employed for lattice relaxation.^[78] Screened hybrid functional HSE06 and spin-orbit coupling SOC were included for accurate electronic structures and improved band gap results. Furthermore, the optical properties were simulated by calculating the dielectric functions of the $MAGeX_3$ compounds, where $X = Cl, Br, I$. **Figure 3** shows the calculated dielectric functions and absorption spectra of $MAPbI_3$, $MASnI_3$, and $MAGeX_3$ systems. Among these materials, $MAGeI_3$ exhibits a nearly overlapping absorption spectrum of $MAPbI_3$ within the visible light region. Although the calculated efficient absorption range of $MASnI_3$ is even larger than $MAPbI_3$ due to its lower optical band gap, $MASnI_3$ is unstable under ambient conditions because of its vulnerability to $Sn^{2+} \rightarrow Sn^{4+}$ oxidation. Based on the calculations on the formation energies of the compounds, $MAGeI_3$ shows better stability than $MASnI_3$. The calculated band structures demonstrate quite dispersive bottom of conduction bands and top of valance bands, which corresponds to low electron/hole effective masses.^[79] These favorable results make $MAGeI_3$ a promising

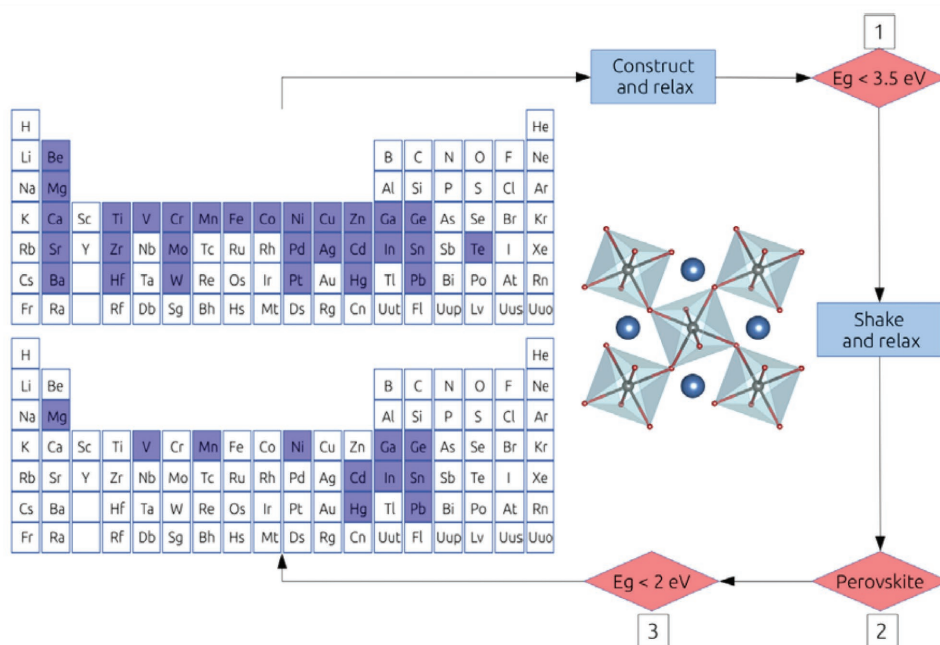


Figure 2. Schematic representation of the computational screening process. The arrows point to the order of the screening steps. The blue shading on the periodic table marks the elements which are considered at the start and at the end of the screening process. The numbers 1, 2, and 3 mark the steps of the screening process at which the number of compound combinations is reduced based on the following criteria: the DFT/LDA scalar relativistic band gap is smaller than 3.5 eV (1), the crystal structure retains the perovskite geometry after relaxation of the shaken configurations (2), and the fully relativistic band gap for the remaining structures is smaller than 2.0 eV (3). The inset shows a ball-and-stick model of the ABX_3 perovskite structure. Reproduced with permission.^[77] Copyright 2015, American Chemical Society.

alternation to $MAPbI_3$, for highly efficient and more environmentally friendly PSCs.

Going beyond the restriction of the classic ABX_3 form, theoretical investigations have been performed on solid solutions with cation and/or anion alloying. Sun et al. used a split-anion approach to investigate the electronic structures of lead-free $MABiXY_2$ compounds, where X is a chalcogen and Y is a halogen to balance the charge.^[80] Ab initio molecular dynamics (AIMD) were performed to study the stability of the systems. GGA functions and DFT-D3 van der Waals scheme were used

for structure relaxation. **Figure 4A** shows the atomic structure of $MABiSeI_2$, which maintained the $MAPbI_3$ tetragonal structure with a freely rotating MA^+ ion according to AIMD simulations. **Figure 4B** compares the band gaps of nine $MABiXY_2$ compounds calculated from a HSE hybrid functional with SOC effect included. Similarly to Pb-based perovskites, $MABiSI_2$ and $MABiSeI_2$ are predicted to have the optimal band gaps (1.3–1.4 eV) for solar energy harvesting materials according to the Shockley–Queisser theory.^[81]

Giorgi et al. theoretically investigated a $MATl_{0.5}Bi_{0.5}I_3$ perovskite, where Tl/Bi aliovalent ionic pairs replace Pb^{2+} cations of $MAPbI_3$.^[82] Although their calculations stayed on the GGA–PBE level, the calculated band gaps of $MATl_{0.5}Bi_{0.5}I_3$ (1.03 eV without SOC and 0.35 eV with SOC) are very promising for further study on this compound. Hong et al. tried to expand the search for quaternary perovskites by allowing more varieties of the chalcogen $X = O/S/Se/Te$ and halogen $Y = F/Cl/Br/I$ in the formula $CsBXY_2$ and $BaBX_2Y$ where $B = Sb/Bi$.^[83] Although some of the compounds exhibited favorable band gap results for solar absorption, the energetic analysis on competing phases predicts that all of these compounds in the family decompose to ternary or binary phases thermodynamically. Despite this unfortunate results, their calculations revealed the importance of stability analysis

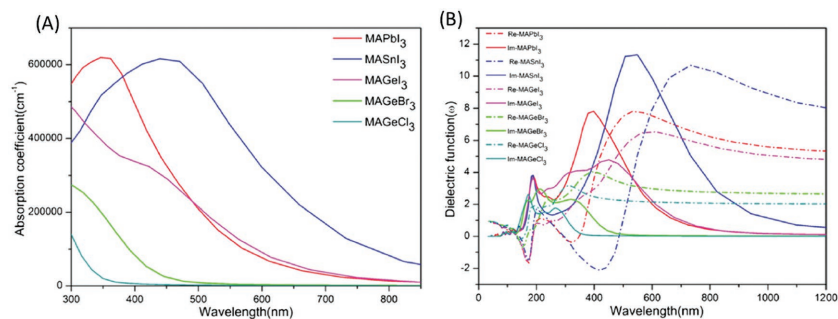


Figure 3. Calculated A) absorption spectra and B) dielectric spectra of the $MAMX_3$ systems. In the dielectric spectra, the imaginary parts are shown in solid lines, and the real parts are shown in dashed lines. Similar conclusions are drawn by comparing the calculated electronic structures and optical properties of $MAPbI_3$, $MASnI_3$, $MAGeI_3$, and $MASrI_3$.^[67] However, in their calculations only GGA functions were included. This might be a result of the cancellation between intrinsic DFT underestimation of band gaps and an effective overestimation without including SOC effects. Reproduced with permission.^[78] Copyright 2016, The Royal Society of Chemistry.

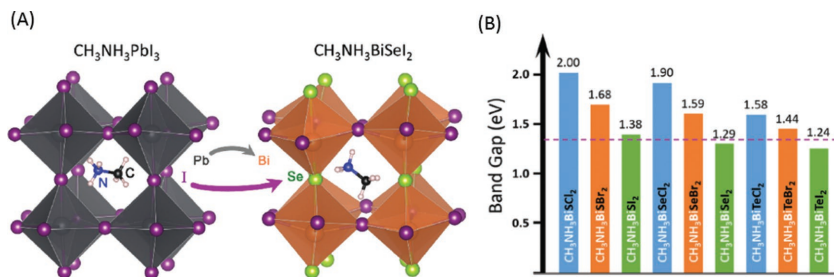


Figure 4. A) Atomic structures of MABiSe_2 and MAPbI_3 . B) HSE-SOC calculated band gaps of MABiXY_2 where X is Te, Se or S and Y is I, Br or Cl. The dashed line marks the optimal band gap for a single-junction solar cell according to the Shockley-Queisser theory. Reproduced with permission.^[80] Copyright 2015, The Royal Society of Chemistry.

for similar calculations aiming for the discovering new lead-free perovskites.

Moreover, Yang et al. broke the restrictions on perovskite structure and tried to develop lead-free solar absorbers from Sb-based semiconductors.^[84] Three antimony sulfides were taken into consideration: Sb_2S_3 with one Dimensional (1D) chained structures, $\text{Cs}_2\text{Sb}_8\text{S}_{13}$ and $\text{MA}_2\text{Sb}_8\text{S}_{13}$ with two Dimensional (2D) layered structures. A HSE06 hybrid functional was used in their calculations and a negligibly weak SOC effect was not included. Although the calculated band gaps are not as impressive (1.72/1.85/2.08 eV for $\text{Sb}_2\text{S}_3/\text{Cs}_2\text{Sb}_8\text{S}_{13}/\text{MA}_2\text{Sb}_8\text{S}_{13}$), the set of the materials are still eligible solar absorbers with a ≈ 0.3 eV tunable gap. The work functions and the ionization potential were also calculated from the electronic structures of their surface states, which shed light on possible contact materials for photovoltaic applications.

3. Experimental Investigation of Organic-Inorganic Hybrid lead-free Perovskite

3.1. Sn-based Perovskite Solar Cells

As a similar element to Pb, tin (Sn) has been reported to be an alternative in lead-free perovskites (both Pb and Sn are belong to IVA group). Pb and Sn have a similar radii of their ion (Pb 1.49 Å and Sn 1.35 Å), which is attributed to the relativistic effect. This might encourage Sn to substitute Pb with no significant perturbation in lattice structure. Besides, Sn-based perovskites have a narrower optical band gap of ≈ 1 eV and a higher charge mobility of $\approx 10^2$ – 10^3 $\text{cm}^2/\text{V}\cdot\text{s}$ (Pb-based perovskite ≈ 10 – 10^2 $\text{cm}^2/\text{V}\cdot\text{s}$).^[85,86] These promising photovoltaic properties can be partly contribute to inactive Sn (II) outer shell orbitals, like inactive Pb 6s orbital in the perovskite structure. However, Sn^{2+} is relatively unstable and easily oxidized to Sn^{4+} leading to self-doping due to a p-type Sn^{4+} act. It might be the primary issue restraining the further advance of Sn-based perovskites while Pb-based perovskites have been improved remarkably. Other views on Sn^{4+} show that there are some reports on a Sn-deficient perovskite derivative based on Sn^{4+} (0-D perovskite derivative). The derivative is indicated to be a semiconductor and exhibits a n-type behavior due to a large ionization potential (IE) and electron affinity (EA) value. More importantly, due to the oxidation nature of Sn, Sn^{4+} shows

more anti-oxidization character compared to Sn^{2+} and is stable in both air and moisture atmospheres.

Therefore, great effort has been done to focus on this new material. Sn-based perovskites have been reported with a lower energy bandgap than Pb-based perovskites in both experimental and theoretical results.^[85,86] Although $\text{MASn}_x\text{Br}_{3-x}$ was synthesis as a non-lead perovskite material in the early 1970s, there was no report that PSCs were realized until Snaith et al. first reported the lead-free MASnI_3 PSCs.^[87] They demonstrated that the crystal of MASnI_3 is highly symmetrical at room temperature which

formed the α -phase of tetragonal $P4mm$ symmetry while MAPbI_3 shows much lower symmetry giving β -phase tetragonal $I4cm$ symmetry in the same condition (Figure 5A, 5B). The MASnI_3 with dark brown color can be obtained without thermal annealing (Figure 5C) while Pb-based perovskites require heating to crystallize. The absorption spectrum of MASnI_3 shows a broad absorption edge at approximately 1000 nm and a broad photoluminescence (PL) peak at 980 nm while the Pb-based perovskites, e.g., MAPbI_3 and $\text{MAPbI}_{3-x}\text{Cl}_x$, give a sharper absorption edge at 770 nm (Figure 5D). The bandgap was estimated at 1.23 eV (Figure 5E), corresponding to the absorption edge and PL spectrum. However, the efficiency obtained is well below that of the lead counterpart. Compared with Pb-based PSCs, Sn-based PSCs showed obvious variation in performance parameters (Figure 5F) and gave a best PCE of only 6.4, 11.5, and 15% for MASnI_3 based on the TiO_2 substrate and $\text{MAPbI}_{3-x}\text{Cl}_x$ based on the TiO_2 and Al_2O_3 substrate, respectively (Figure 5G). The poor performance may be attributed to the low PL lifetime of 200 ps compared to the long-lived charge carriers up to a few hundred nanoseconds for $\text{MAPbI}_{3-x}\text{Cl}_x$ and at least 10 ns for the MAPbI_3 perovskite. The fast PL decay was related to the fast recombination of carriers at defects born with the material. Moreover, it has been reported that Sn^{2+} is easily oxidized to Sn^{4+} , which play a role in p-type doping of the material resulting in the limited photoexcited carriers diffusion length and the charge extraction in the device.

Independent to the Snaith work, Kanatzidis et al. reported Sn-based perovskites by partial chemical substitution of I^- by Br^- forming $\text{MASnI}_{3-x}\text{Br}_x$ perovskites (Figure 6A),^[88] which can be controllably tuned to cover much of the visible spectrum. The absorption onset shows a blue shift from 950 nm (MASnI_3) to 577 nm (MASnBr_3) with an increase in the number x , leading to the color of the film changing from dark brown to transparent yellow (Figure 6B and Figure 6C). The bandgap of MASnI_3 fixed at 1.3 eV was achieved (Figure 6D), corresponding to the literature reported by Snaith et al.^[87] They found that the V_{oc} and fill factor (FF) were significantly increased upon the incorporation of the Br^- from MASnI_3 to MASnBr_3 , which can be attributed to the raised conduction band-edge (Figure 6D) and reduced series resistance with increasing Br content in $\text{MASnI}_{3-x}\text{Br}_x$ perovskites. Since the E_g is increased with an increase of Br^- in $\text{MASnI}_{3-x}\text{Br}_x$ as is well known in Pb-based perovskites such as $\text{MAPbI}_{3-x}\text{Br}_x$ due to the reduced ion radius of Br^- compared to I^- .^[89] Accordingly,

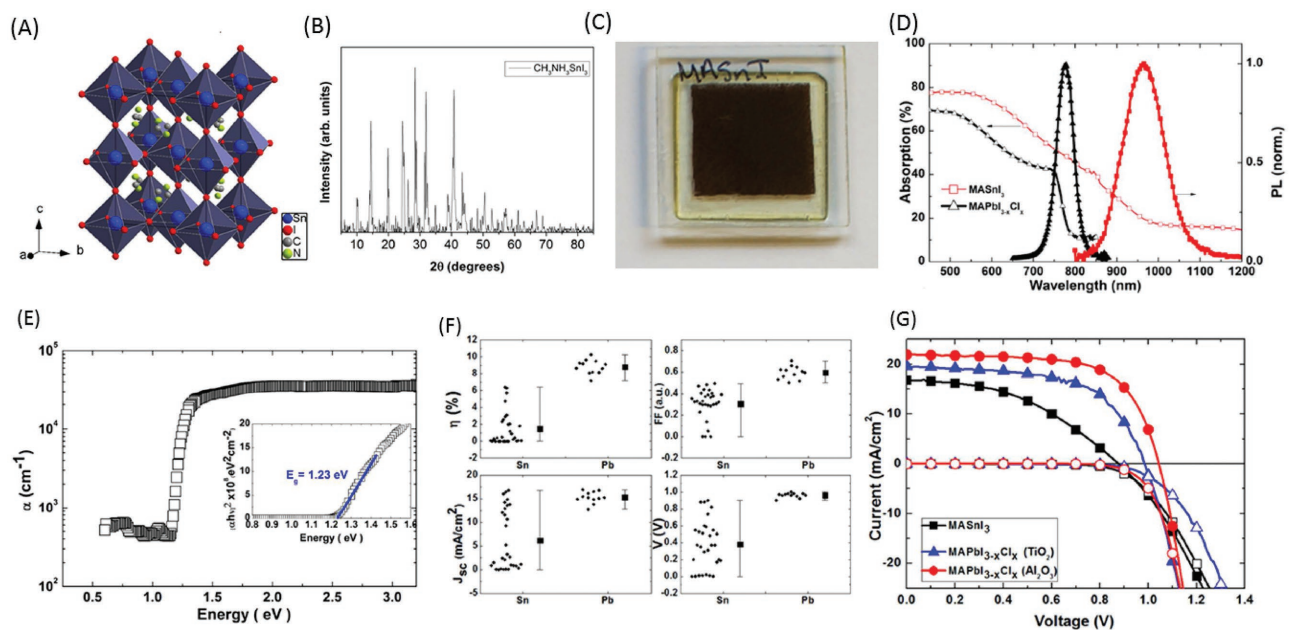


Figure 5. A) The crystal structure of MASnI_3 with the tetragonal conformation. B) XRD spectrum of MASnI_3 film. C) Picture of the dark brown film of MASnI_3 encapsulated in the internal atmosphere. D) Normalized photoluminescence (PL) and absorption spectrum for MASnI_3 and $\text{MAPbI}_{3-x}\text{Cl}_x$ respectively. E) Photo-thermal deflection spectroscopy (PDS) of MASnI_3 with 1.23 eV bandgap obtained from Tauc plot (inset). F) PCE, FF, J_{sc} and V_{oc} parameters of devices performance for Sn-based and Pb-based PSCs both of which employ TiO_2 as substrate. G) J - V curve under AM 1.5 simulated sun light for devices fabricated with MASnI_3 based on the TiO_2 substrate (black curve) and $\text{MAPbI}_{3-x}\text{Cl}_x$ based on the TiO_2 (blue curve) and Al_2O_3 substrate (red curve) with PCE of 6.4, 11.5, and 15%, respectively. Reproduced with permission.^[80] Copyright 2013, The Royal Society of Chemistry.

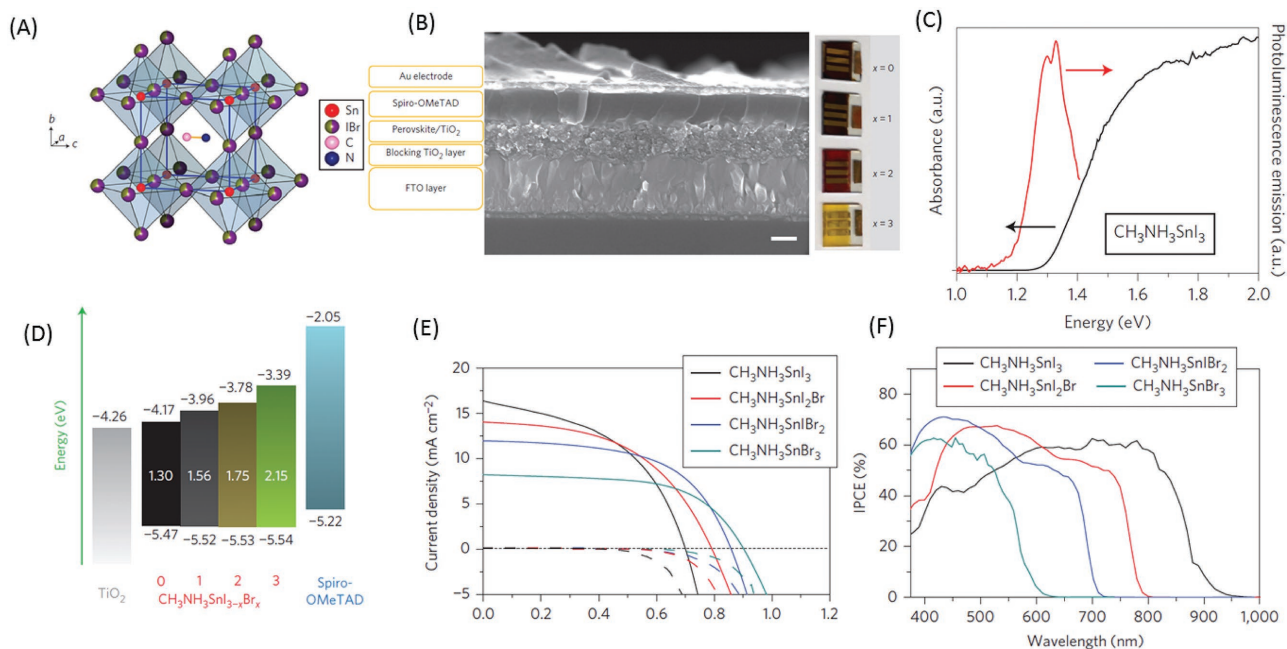


Figure 6. A) Crystal structure of $\text{MASnI}_3\text{Br}_{3-x}$ perovskite. B) the cross-sectional Scanning Electron Microscope (SEM) image of $\text{MASnI}_3\text{Br}_{3-x}$ left and the film images of different incorporation of stoichiometry of Br ($x = 0, 1, 2, 3$) showing a well penetrated perovskite film deposited on the mesoporous TiO_2 substrates. However, Some pinhole still distributed on the film may lead to a impact in device performance finally. C) Photoluminescence and absorption spectrum for MASnI_3 . D) Energy-level diagram of $\text{MASnI}_3\text{Br}_{3-x}$ With spiro-OMeTAD and TiO_2 . E) The J - V curve of $\text{MASnI}_3\text{Br}_{3-x}$ PSCs devices at different ratio of Br/I in which $\text{MASnI}_3\text{Br}_2$ reach highest PCE of $\approx 5.73\%$. F) IPCE spectrum for $\text{MASnI}_3\text{Br}_{3-x}$ solar cells devices showing a blue-shift of onset with the increasing ratio of Br/I that corresponds with devices in (E). Reproduced with permission.^[88] Copyright 2014, Macmillan Publishing.

the ability of light-harvesting is decreased with increasing ratio of Br^- , leading to the decrease of J_{sc} . (Figure 6e) By perovskite chemical compositional engineering, $\text{MASnI}_{3-x}\text{Br}_x$ can be proved to be an active layer in the PSCs and they have finally achieved an optimized device by employing the MASnIBr_2 perovskite with the best PCE of $\approx 5.73\%$ (Figure 6E) and IPCE response over 900 nm (Figure 6F).

The homogeneity and coverage of the MASnI_3 perovskite film is another limiting factor for high performance, which may result in a high frequency of shunt paths allowing direct contact between the hole-transporting layer (HTL) and electron-transporting layer (ETL), deteriorating the FF and V_{oc} .^[88,89] Poor film coverage with the presence of pinholes is related to uncontrollable crystallization during the solution-based deposition process, a behavior which is notably different from the lead analogue.^[90] Compared to the numerous studies on the morphological control of MAPbI_3 film growth,^[91–98] investigation on the tin counterparts are highly limited due to the fact that experiments are typically hampered by rapid oxidation of Sn^{2+} under ambient conditions, which requires an inert dry atmosphere. Kanatzidis et al. found that solvent evaporation effects are detrimental to obtaining uniform, pinhole-free MASnI_3 perovskite film since the faster reaction rate between the two halide precursors SnI_2 and MAI than the MAPbI_3 analogue. The quality of films thus can be greatly improved through solvent engineering (Figure 7A).^[99] They systematically investigated four commonly used highly polar solvents, dimethyl sulfoxide (DMSO), N,N-dimethylformamide (DMF), N-methyl-2-pyrrolidone (NMP), and γ -butyrolactone (GBL) to compare the crystallization processes for MASnI_3 perovskite films.^[100] The stabilization of the

intermediate SnI_2 solvates by solvents is dominant and promotes homogeneous nucleation, and enables an adjustable perovskite film growth rate. High-quality, pinhole-free MASnI_3 films were achieved using DMSO and NMP as solvents since they can induce an intermediate phase (e.g., $\text{SnI}_2 \cdot 3\text{DMSO}$) which plays an important role in controlling the crystallization process and final thin film quality (Figure 7B, 7C, 7D, and 7E). Finally, an unprecedented photocurrent density up to 21 mA cm^{-2} was obtained in DMSO-based perovskite film. Moreover, they demonstrated that the film growth of MASnI_3 can be successfully controlled using low temperature vapor assisted solution process (LT-VASP) by modifying the conventional VASP method.^[101,102] The substrate temperature ($60\text{--}80^\circ\text{C}$) during VASP is a key parameter in achieving high quality MASnI_3 films and MASnI_3 perovskite can be formed in a minute timescale which is much faster than that in the Pb-analogue (Figure 7F).^[102] A drastic improvement in film surface coverage was obtained in the LT-VASP film compared to a conventional VASP film (Figure 7G and 7H). Devices fabricated by the LT-VASP method show the best PCE reaching 1.86% with drastically improved reproducibility. Another room-temperature MASnI_3 film fabrication method in dry atmosphere was investigated by the Ogale group via pulse excimer laser deposition,^[103] which is widely utilized for nitrides, inorganic, and polymer systems. High quality films can be obtained by reducing the decomposition of the moisture-sensitive perovskite.

Very recently, Schlettwein et al. demonstrated a thermal evaporation involved solution-processed approach to fabricate a MASnI_3 perovskite film similar to the previous report of a $\text{MAPbI}_x\text{Cl}_{3-x}$ perovskite film.^[15,104] Briefly, tin(II) iodide (SnI_2) layers prepared by physical vapor deposition were converted to

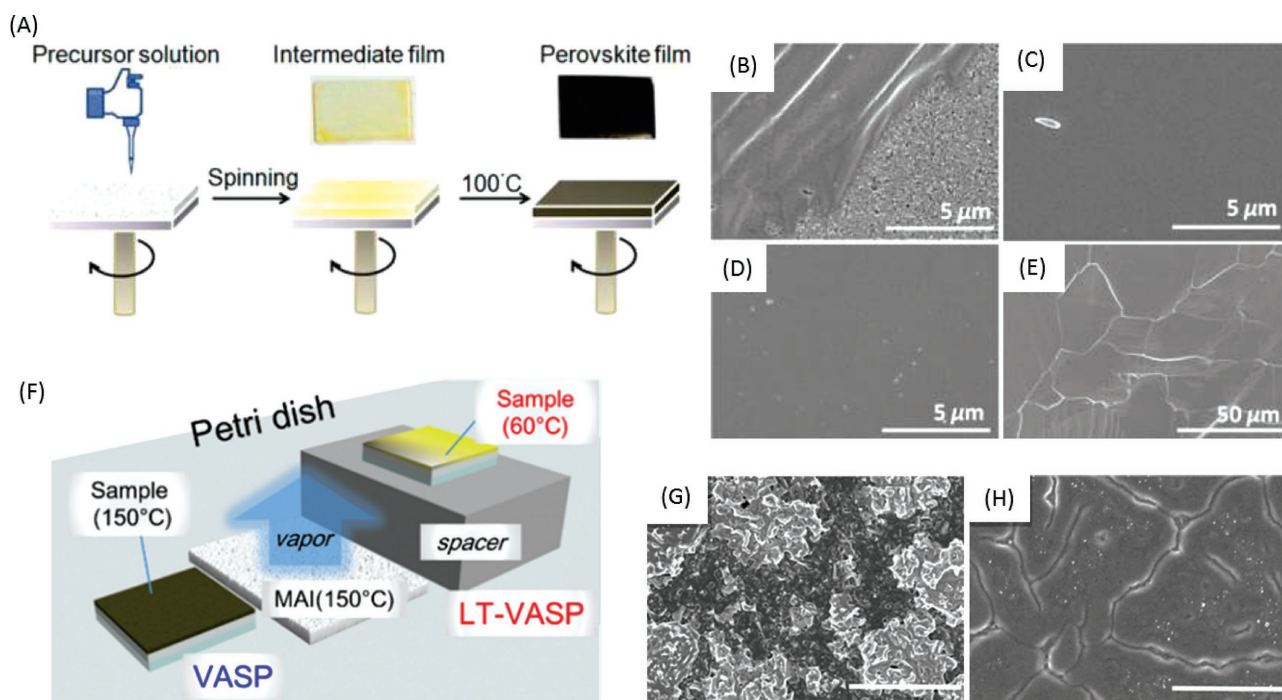


Figure 7. A) One-step method for MASnI_3 film deposition with DMSO as solvent. SEM images for MASnI_3 layer on the mesoporous TiO_2 layer from B) DMF, C) NMP, D) GBL, and E) DMSO (different magnification) solvents.^[107] F) Schematic of LT-VASP and VASP. SEM images for MASnI_3 films with different process of G) VASP and H) LT-VASP. A–E) Reproduced with permission.^[99] Copyright 2015, American Chemical Society. F–H) Reproduced with permission.^[102] Copyright 2016, American Chemical Society.

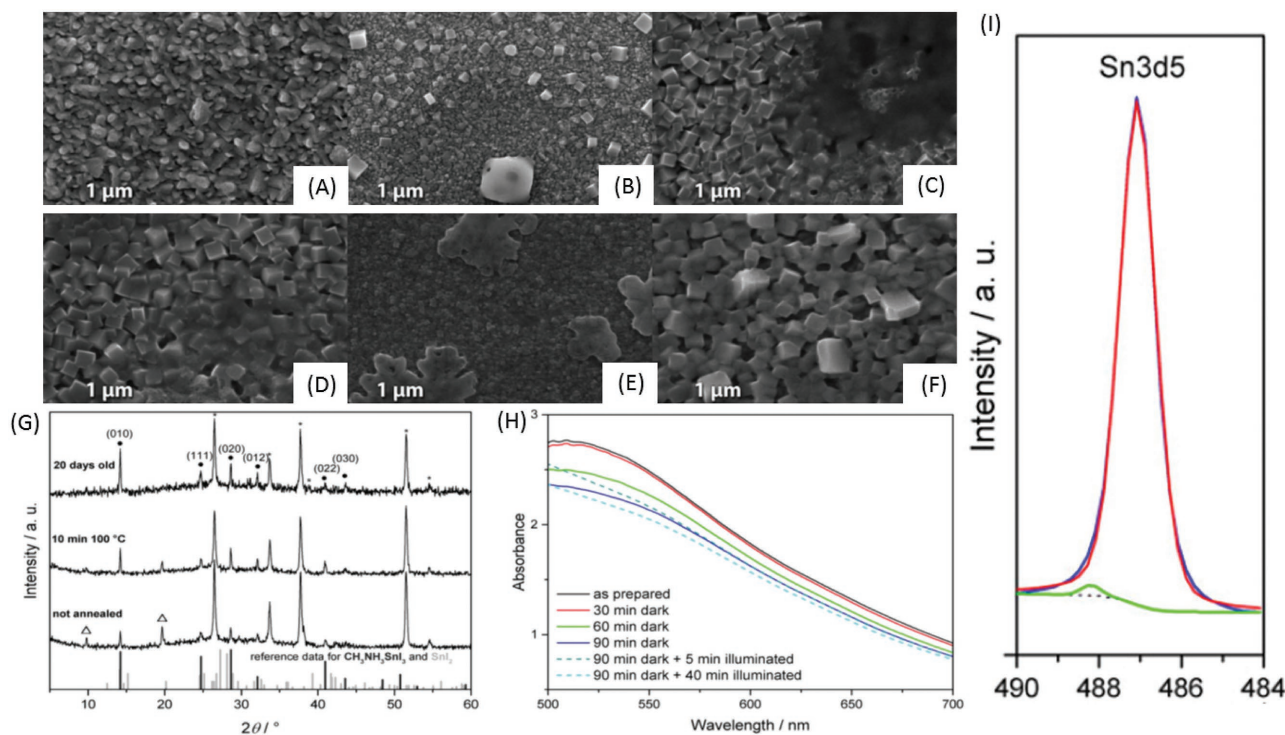


Figure 8. SEM images of A) vapor deposited 100 nm SnI₂, non-annealing MASnI₃ films with B) 6 mg mL⁻¹, C) 10 mg mL⁻¹, D) 20 mg mL⁻¹ and E) 40 mg mL⁻¹ precursor MAI solution spin coated and F) MASnI₃ films with 20 mg mL⁻¹ precursor MAI solution spin coated followed by annealing at 80 °C for 10 min. G) XRD spectrum at different times of MASnI₃ films with 20 mg mL⁻¹ precursor MAI solution spin coated. H) stability of MASnI₃ film stored in air. I) Narrow scan of XPS pattern of MASnI₃ films with 20 mg mL⁻¹ precursor MAI solution spin coated. Reproduced with permission.^[104] Copyright 2015, Wiley-VCH Verlag GmbH & Co. KGaA, Weinheim.

MASnI₃ by reaction with a spin-coated solution of MAI. They found that the perovskite particles formed in this process were over 200 nm in size and reached full surface coverage since the evaporated SnI₂ (Figure 8A) already fully covers the substrate compared to that of solution processing.^[87,88] Moreover, it showed that annealing is not necessary for the resulting MASnI₃ films corresponding to the previous report.^[87] The morphology was highly dependent to MAI concentrations, as shown in Figure 8A, B, C, D and E, where increasing the MAI concentrations saw the distribution of MASnI₃ crystals as more uniform with increased mean crystallite size (e.g., 20 mg mL⁻¹) and then reduced with further increasing MAI concentration to 40 mg mL⁻¹. By annealing, however, the crystallites sintered together even for short periods of time (10 min) at low temperatures (80 °C) (Figure 8F). More importantly, the fabricated MASnI₃ did not show any Sn⁴⁺ peaks upon annealing or storage for 20 d in a glove box, indicating the material's superior stability (Figure 8G). This was further confirmed by the main peak at 487 eV assigned to Sn²⁺ whereas a small additional signal around 488 eV caused by the presence of Sn⁴⁺ at a content (< 1%) in the Sn3d₅ peak (Figure 8I). Moreover, the film still exhibited great stability when exposed to air for up to 90 min both under dark and light, which is significantly superior to earlier reports in stability. (Figure 8H).^[87,88] The improved stability may be attributed to the high-quality and dense thermal evaporated SnI₂ film as seen in a previous report using thermal evaporated PbCl₂ in fabricating a MAPbI_xCl_{3-x} perovskite film with enhanced stability compared to the solution processed method.^[15]

Accordingly, co-evaporation and sequential evaporation were subsequently demonstrated by Qi et al. to fabricate MASnBr₃ perovskite films using SnBr₂ and MABr precursors.^[105] The co-evaporated PSCs gave lower efficiency (0.35%, Figure 9A) due to the fast formation of Sn-Br oxide on the top surface during the fabrication process (Figure 9B and 9C). It is because the oxidation of Sn can lead to Sn vacancies in the lattice structure of MASnBr₃ (the three Dimensional (3D) perovskite structure transferred into 0 Dimension (0D)), which results in the metallic conductivity of the materials.^[106-110] The capping Sn-Br oxide layer restrains the generation of excitons, the transport of holes and electrons, and the extraction of electrons due to its p-type characteristic, leading to the low efficiency. On the other hand, MASnBr₃ perovskite films made by sequential deposition (Figure 9D) exhibited a higher efficiency (1.12%, Figure 9E) than those made by the co-evaporated method because air-induced oxidation can be significantly avoided by the top MABr layer. Therefore, sequential deposition both in solution and thermal evaporation approach could be an effect approach in fabricating Sn-based perovskites.

Compared to MA⁺, FA⁺ is another highly investigated organic cation counterpart with a relatively larger radius and was confirmed to form a 3D perovskite with a lower bandgap of about 1.47 eV in FAPbI₃ as compared to MAPbI₃ (1.57 eV).^[23] The organic cation was considered as not taking part in determining the band structure, but works to fulfill charge neutrality within the lattice.^[107] However, its size is quite vital. The size of the organic cation can cause the entire network to enlarge

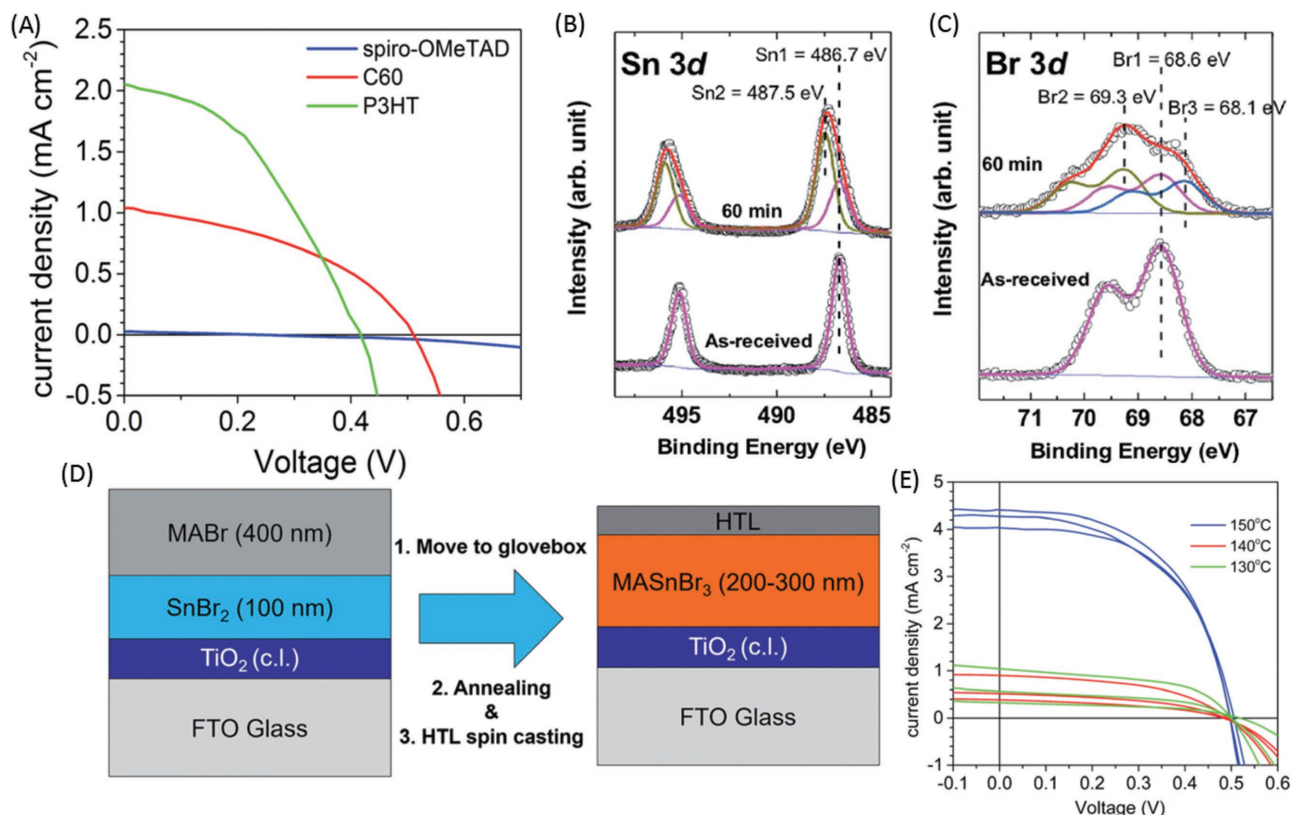


Figure 9. A) *J*–*V* curves of co-evaporated MASnBr₃ films with different HTMs. B) and C) Stability of MASnBr₃ films as-deposited and after 60 min stored in air. D) Fabrication of sequential method for MASnBr₃ films. E) *J*–*V* curves of sequential deposited MASnBr₃ films, annealed at different temperatures. Reproduced with permission.^[105] Copyright 2016, The Royal Society of Chemistry.

or be compressed. Very recently, Mathew et al. reported formamidinium tin iodide (FASnI₃) as a light absorber for solar cell applications. The FASnI₃ shows an energy band gap of 1.41 eV, which is smaller than those of lead-based perovskite light absorbers FAPbI₃ (1.47 eV) (Figure 10A),^[108] and has an orthorhombic (Amm2) crystal structure according to XRD patterns (Figure 10B). Moreover, no phase transition was observed as evident by the same XRD peaks of the samples prepared by annealing at different temperatures from 100 to 200 °C, which is highly different from the analogous lead compound FAPbI₃ possessing perovskite black polymorphs and non-perovskite yellow polymorph.^[26,106,112,113] Most importantly, the SnF₂ was used as an additive to prevent Sn²⁺ from being oxidized to Sn⁴⁺ and to reduce the background carrier density in FASnI₃ perovskites.^[22] The oxidation was totally prohibited as demonstrated from XPS spectra (Figure 10C), in which no Sn⁴⁺ peaks were found, and the morphology of the FASnI₃ perovskite can be further improved as shown in Figure 10D, E and F. The surface coverage was significantly enhanced with additional 10–20% SnF₂ while nanoplatelet-like structures were observed on the perovskite surface with increasing concentration of SnF₂ to 30–40%. Accordingly, the optimum PCE of 2.1% was obtained with a concentration for SnF₂ of 20%.

As demonstrated, SnF₂ is necessary to stabilize FASnI₃ perovskites and improve quality; however, a higher amount of SnF₂ induces severe phase separation in the film, interrupting the improvement in the efficiency of the device. Therefore, it

is very important to further improve the FASnI₃ film quality with regards to obtaining a uniform and dense perovskite layer without any phase separation and micrometer sized aggregates. Seok et al. reported an effective approach to bind SnF₂ well with pyrazine by accepting lone pairs from the N atoms in pyrazine, which can remarkably restrict the phase separation induced by the excess SnF₂ and reduce the Sn vacancies effectively. The additional introduction of pyrazine into the solution by solvent engineering (DMF and DMSO mixture solvent at volume ratio of 4:1), as demonstrated by Kanatzidis et al.,^[106] led to a smooth, dense, and pinhole-free FASnI₃ perovskite layer (Figure 11A and B) while the solution without pyrazine gave films with some plate-like aggregates. This implies that the phase separation was significantly reduced by forming SnF₂/pyrazine complex and the surface morphology of the FASnI₃ perovskite film can be finally improved. Moreover, the addition of pyrazine does not change the crystal structure as compared with that without pyrazine since it can be easily removed because of its low boiling point of 115 °C during the annealing process (Figure 11C). Therefore, the PCE was significantly improved by improving the *V*_{oc}, *J*_{sc}, and FF (Figure 11D). Finally, the highest reported PCE of 4.8% and IPCE for FASnI₃ PSCs was achieved with high reproducibility (Figure 11E, F and G). Most importantly, the encapsulated cells showed good stability for over 100 d under ambient condition (Figure 11H), showing long-term stability remaining 98% initial PCE with no obvious decomposition contrasting with the oxygen-sensitive

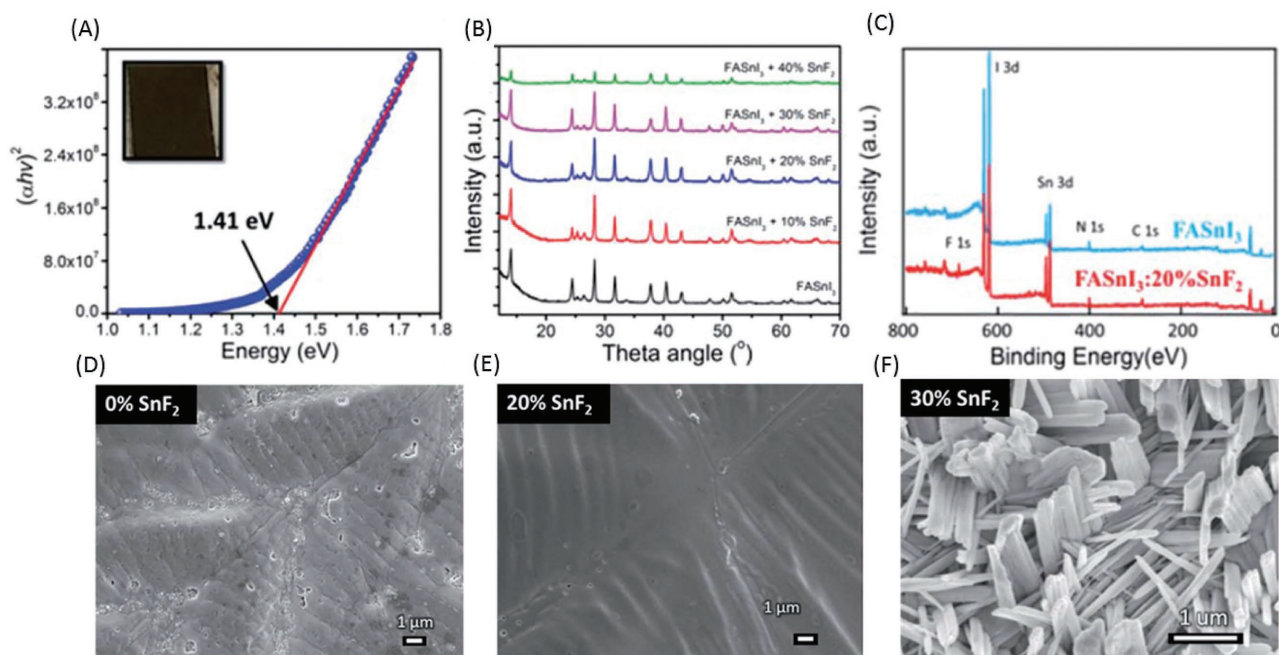


Figure 10. A) Tauc plot of MASnI₃ Film with optical absorption onset of 1.41 eV. B) XRD pattern of MASnI₃ with different SnF₂ additive ratio of SnF₂ (mol%). C) XPS spectrum of MASnI₃ and MASnI₃: 20% SnF₂ Films. SEM images of MASnI₃ with different SnF₂ additive ratio, D) 0%, E) 20%, and F) 30%. Reproduced with permission.^[111] Copyright 2015, The Royal Society of Chemistry.

Sn-based perovskite. This paves a new way for the development of stable Sn-based perovskites and sheds light on the establishment of high efficient and stable lead-free PSCs.

Very recently, Zhao et al. further improved the performance of FASnI₃-based perovskite solar cells using an inverted structure (Figure 12A).^[113] This is because they recognized that the

lithium (Li) and/or cobalt (Co) salts, which are needed to dope hole transporting materials in the regular structure, could damage the Sn-based perovskite films and lead to poor device performance. In the basic works by Kanatzidis and Seok,^[106,112] they obtained high-quality, uniform, and fully covered FASnI₃ perovskite thin films employing diethyl ether to replace the

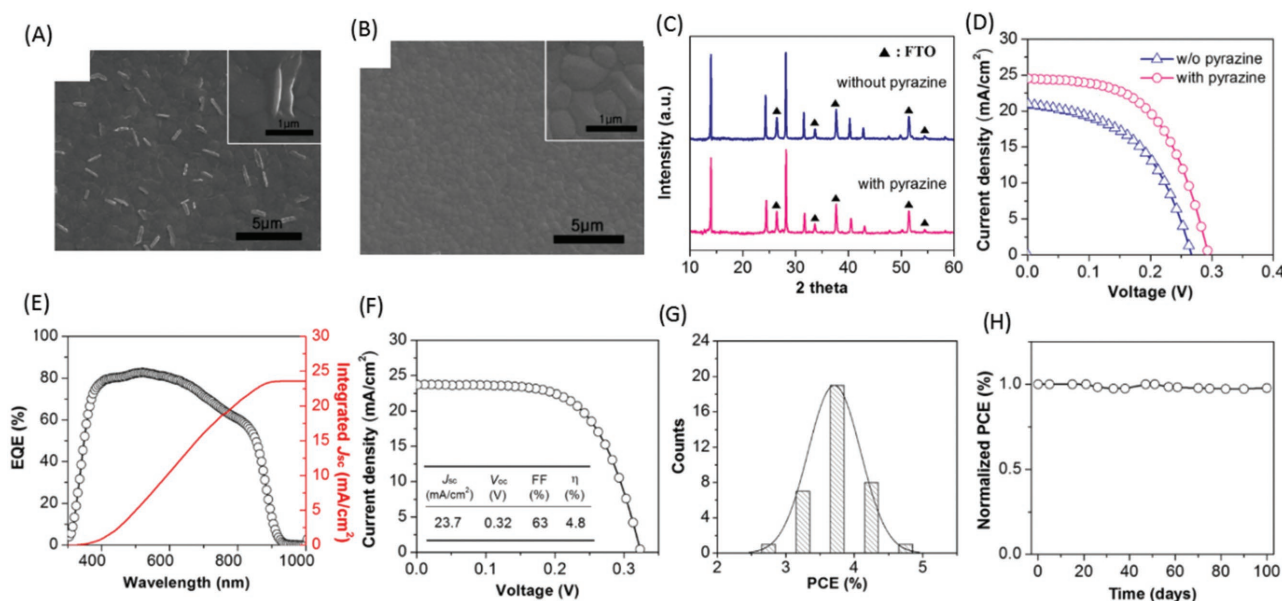


Figure 11. SEM images of FASnI₃ perovskite films A) with pyrazine and B) without pyrazine in precursor solution. C) XRD pattern of FASnI₃ perovskite films with and without pyrazine. D) J–V curve of FASnI₃ PSCs with and without pyrazine. E) EQE, integrated J_{sc} and F) J–V curve of optimized FASnI₃ PSCs. G) Pattern of PCE obtained from 36 devices. H) Stability of encapsulated FASnI₃ PSCs under ambient condition for over 100 d. Reproduced with permission.^[107] Copyright 2016, American Chemical Society.

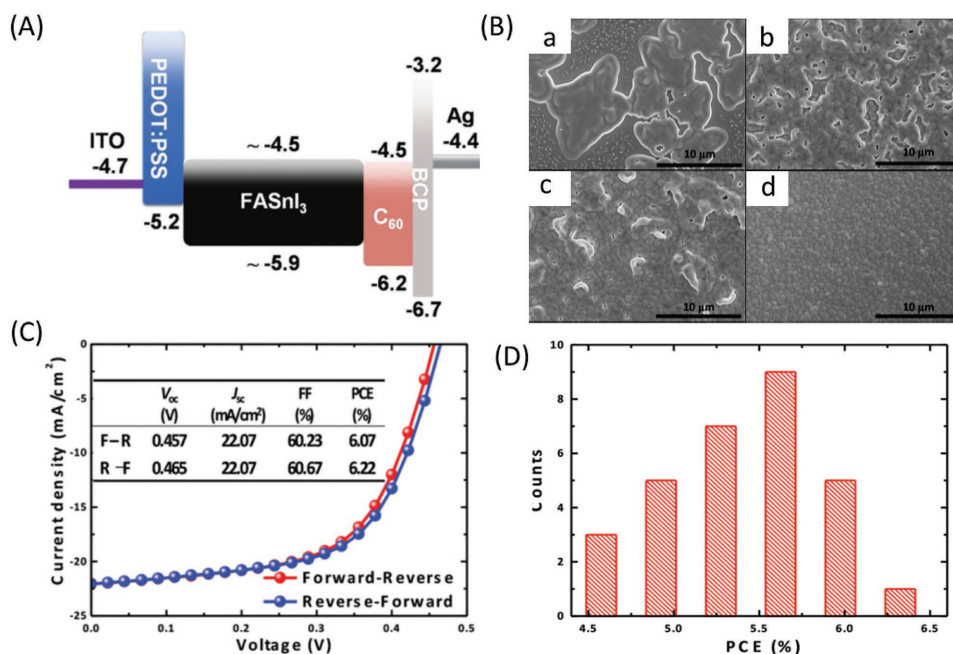


Figure 12. A) Energy level pattern of FASnI₃ solar cells. B) SEM images of FASnI₃ films obtained from different antisolvent processes: a. No dripping, b. Chlorobenzene, c. Toluene and d. diethyl ether. C) *J-V* curves of FASnI₃ solar cells with very small *J-V* hysteresis behavior. D) PCE pattern obtained from 30 devices with 10% SnF₂ additives incorporation. Reproduced with permission.^[113] Copyright 2016, Wiley-VCH Verlag GmbH & Co. KGaA, Weinheim.

popular chlorobenzene and toluene in a solvent engineering process. As shown in Figure 12B, dripping with chlorobenzene improved the surface coverage of the FASnI₃ films with hierarchical morphology with rougher surface and pinholes compared to that without antisolvent dripping. Dripping with toluene further improved the coverage of the FASnI₃ perovskite films by the fact that pinholes remained and the surface is rough due to island formation. Dripping with diethyl ether; however, produced the best FASnI₃ thin films being highly uniform and completely covering the substrate. Due to the improved film quality and proper structure design, the champion FASnI₃ device achieved a maximum PCE of 6.22% with a V_{oc} of 0.465 V, a J_{sc} of 22.07 mA cm⁻², and an FF of 60.67% under forward voltage scan and exhibited very small *J-V* hysteresis behavior (Figure 12C). Moreover, the devices appeared to be highly reproducible (Figure 12D). However, the PCEs are highly limited by the V_{oc} s, which could be ascribed to the charge carrier imbalance resulting from the interfacial barriers at the interface between charge transport layers and the FASnI₃

perovskite layer (Figure 12A). If a similar V_{oc} reported by Snaith (0.88 eV) was obtained, PCEs over 10% should be expected.

As the only suitable metal ion Cs⁺ in 3D perovskite structure according to the tolerance factor *t*, cesium tin halides (e.g., CsSnI₃) have recently been intensively investigated. CsSnI₃ is a 3D p-type orthorhombic perovskite with a bandgap of 1.3 eV,^[107,114] high optical absorption coefficient (10⁴ cm⁻¹ comparable to MAPbI₃),^[115] and low exciton binding energies (18 meV),^[116] indicating that it is a viable candidate as a light absorber for lead-free PSCs. Shum et al. first described a CsSnI₃ perovskite based Schottky solar cell with the structure of ITO/CsSnI₃/Au/Ti in the early half of 2012, as shown in Figure 13A.^[117] The thin-film synthesized by alternately depositing layers of SnCl₂ and CsI on a glass substrate followed by a thermal annealing process converting the SnCl₂/CsI stack to a black thin-film of CsSnI₃, which had an intense PL peak at 950 nm corresponding to the low bandgap of 1.3 eV (Figure 13B). The device gave the best PCE of 0.9%; however, it is limited by high series and shunt resistance (Figure 13C).

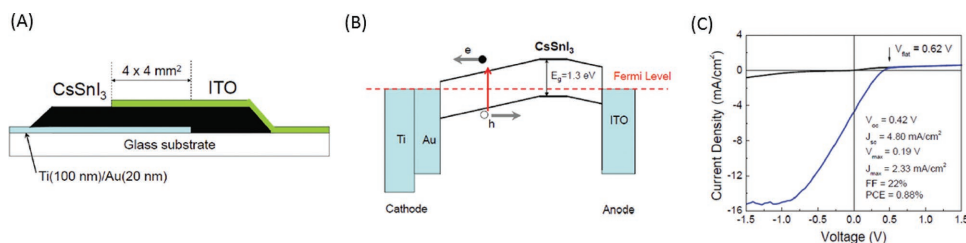


Figure 13. A) Schematic, B) Energy-level pattern and C) *J-V* curve of CsSnI₃-based Schottky solar cells. Reproduced with permission.^[117] Copyright 2012, American Institute of Physics.

Although the PCE for this prototype solar cell based on CsSnI_3 is only near 1%, they claimed that it provides a promising platform for thin-film based solar cells.

In fact, CsSnI_3 is prone to form intrinsic defects associated with Sn-cation vacancies, which intensively limits the photocurrent.^[115] Mathews et al. reported that high photocurrent can be achieved in a CsSnI_3 PSC with SnF_2 incorporation through the reduction of the Sn vacancies. From the similar XRD patterns of films with 0, 5, 10, 20, and 40 mol% SnF_2 in CsSnI_3 perovskite films (Figure 14A),^[108] we can clearly see that SnF_2 cannot incorporate into the CsSnI_3 perovskite lattice due to the much smaller ionic radii of F^- (1.33 Å) compared to I^- (2.20 Å) corresponding to the literature.^[22,106] The presence of F^- within the film was confirmed by XPS measurements by comparison of pristine CsSnI_3 and 20 mol% SnF_2 - CsSnI_3 (Figure 14B). The addition of SnF_2 actually eliminates the unknown reflections caused by the yellow polymorph phase of an impurity. The best PCE was finally obtained for 20% SnF_2 - CsSnI_3 with $J_{\text{sc}} = 22.70 \text{ mA cm}^{-2}$, $V_{\text{oc}} = 0.24 \text{ V}$ and $\text{FF} = 0.37$ which resulted in $\eta = 2.02\%$ (Figure 14C). Moreover, the devices displayed less hysteresis (Figure 14D). The IPCE data clearly indicated that the onset is extended to 950 nm corresponding to the absorption onset with infrared response (Figure 14E). Most importantly, the device showed great stability for more than 250 hr inside a glovebox (Figure 14F), which may open up new possibilities of exploiting lead-free perovskites via the point of view of stability.

Although the stability of CsSnI_3 based PSCs improved a lot inside a glovebox, the notorious property of air sensitivity of Sn perovskites still remains with the black phase converting

to yellow phase CsSnI_3 under atmosphere, which in turn oxidizes to Cs_2SnI_6 in which Sn is in its more stable +4 oxidation state.^[85,107] Hatton et al. reported an effective strategy for simultaneously improving both the efficiency and stability of CsSnI_3 based PSCs towards air exposure with an excess of SnI_2 during CsSnI_3 growth from CsI and SnI_2 .^[118] The p-i-n device with a configuration of ITO/CuI/ CsSnI_3 /fullerene/BCP/Al, as shown in Figure 15A. The orthorhombic CsSnI_3 films can be prepared from solution at room temperature with defect densities low enough on the CuI hole transporting layer for the first time. It was remarkably different from previous reports, which CsSnI_3 films with low defect density were prepared in a Sn rich environment or at high temperature.^[35,106] It can be seen from the SEM images of the CsSnI_3 film shown in Figure 15B and C, the film is made up of small crystals $\approx 100 \text{ nm}$ in diameter with high surface coverage, which is highly impressive in just a 50 nm thick film. As shown in Figure 15D, the PCE of the device exhibits a significant increase with an excess of SnI_2 , and the optimal 10 mol% SnI_2 led to a doubling of the PCE from 0.75 to 1.5%. Moreover, the device showed a negligible hysteresis effect (Figure 15E). They recognized that the excess of SnI_2 was actually buried at the CsSnI_3 /CuI interface and acted as a hole transporting layer from CsSnI_3 to CuI with a favorable vacuum level shift at the interface due to the formation of an interfacial dipole. The device stability was also investigated under an unencapsulated condition as a function of the SnI_2 excess in the CsSnI_3 layer, as shown in Figure 15F. The data points in the hashed region correspond to device performance immediately after fabrication and after storage for

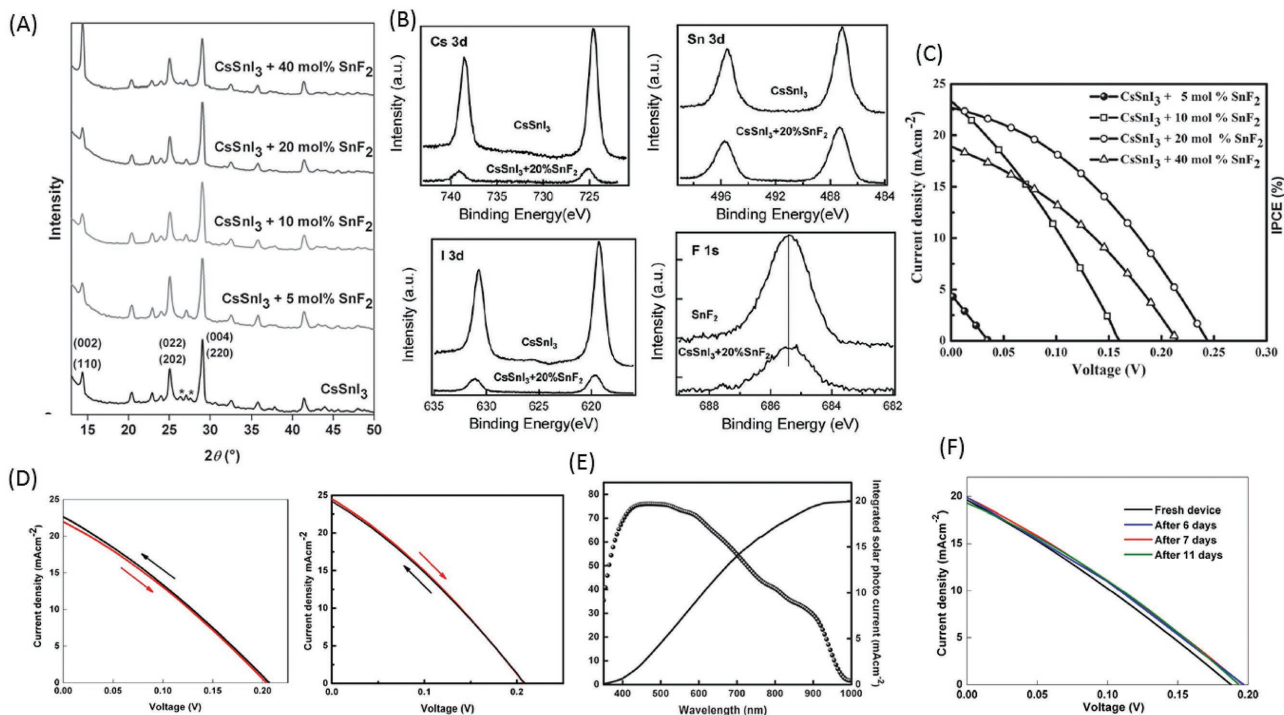


Figure 14. A) XRD pattern of CsSnI_3 with different ratio SnF_2 doping. B) XPS narrow scan for F 1s, I 3d, Sn 3d and Cs 3d. C) J - V curves of PSCs with different ratio SnF_2 incorporation. D) J - V curves of CsSnI_3 : 20 mol% SnF_2 devices obtained from both negative to positive and positive to negative direction showing no hysteresis. E) IPCE spectrum for CsSnI_3 : 20 mol% SnF_2 devices. F) Stability of devices obtain from J - V curve on different days. Reproduced with permission.^[108] Copyright 2014, Wiley-VCH Verlag GmbH & Co. KGaA, Weinheim.

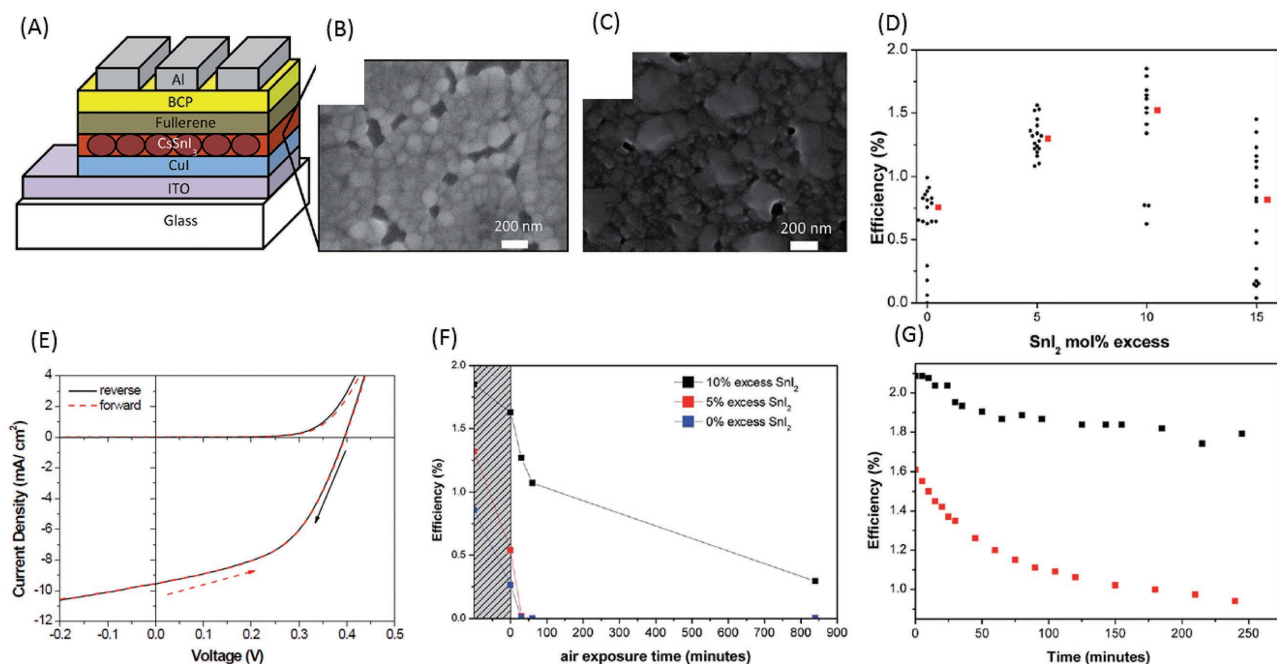


Figure 15. A) Device structure of CsSnI₃-based PSCs. SEM images of B) 8 wt% and C) 15 wt% CsSnI₃: 10 mol% excess SnI₂ films. D) Scatter pattern of PSCs performance with the structure of ITO/CuI/CsSnI₃/fullerene/BCP/Al at different ratios of excess SnI₂. E) *J*-*V* curve of devices with this structure showing negligible hysteresis. F) Stability of these devices stored in a nitrogen atmosphere for 10 d followed by being stored in air (the performance was obtained as a function of time stored in air). G) Illumination effect (100 mW cm⁻² of AM 1.5) for 245 min to the devices with 0% (red) and 10% (black) excess SnI₂. Reproduced with permission.^[118] Copyright 2015, The Royal Society of Chemistry.

10 d in a nitrogen filled glove box. Devices based on CsSnI₃ with 10 mol% excess SnI₂ exhibit a relatively small reduction in PCE while devices based on CsSnI₃ films prepared using stoichiometric amounts of CsI and SnI₂ showed that the PCE is reduced by 70% after a 10 day period of storage. Devices with 10 mol% excess SnI₂ still exhibited dramatically improved stability even after 14 hr in air without encapsulation while devices with 0 mol% excess SnI₂ stopped working after 30 min air exposure. Moreover, the stability of devices with 10 mol% excess SnI₂ in the CsSnI₃ layer exhibited illumination stability over a period of 4 hr continuous illumination in a nitrogen atmosphere, as shown in Figure 15G.

As shown, the *V*_{oc} was highly limited to below 0.3 V in CsSnI₃ based devices and is attributed to the high background carrier density due to Sn-vacancy defects even when prepared under Sn-rich conditions.^[108] Therefore, the Mathews group further demonstrated that substitution of I⁻ by Br⁻ in CsSnI₃ forming CsSnI_{3-x}Br_x perovskites is an effective approach of increasing the *V*_{oc} over 0.4 V.^[119] The *V*_{oc} enhancement is due to the decrease in Sn vacancies and a high resistance to charge recombination in CsSnI_{3-x}Br_x perovskites (Figure 16A and B). The shunt resistances corresponding to the recombination resistance turn to higher parameters with increasing Br ratio in CsSnI_{3-x}Br_x. With increasing the Br content, furthermore, the band gap shift over 0.4 eV from CsSnI₃ to CsSnBr₃ (Figure 16C) accompanied by crystal structure transition from orthorhombic to cubic configuration with color variation from black to light-brown (Figure 16D). However, improvement in *V*_{oc} was at the expense of photocurrent due to the relevant blue shift in the absorption spectrum besides the higher *E*_g (Figure 16E), which

corresponds to the case from MAPbI₃ to MAPbBr₃.^[18] In addition, the Br-rich samples show a perfectly linear dependence of *J*_{sc} against light intensity while I-rich samples show a nearly linear dependence (Figure 16F). This phenomenon is correlated with the decrease of most defects of CsSnI₃. Moreover, it is worth noting that the Br-based CsSnI_{3-x}Br_x perovskites show a much higher FF compared with CsSnI₃ due to the appearance of the negligible overlayer of CsSnI_{3-x}Br_x.^[119]

Very recently, Sun et al. carefully compared mesoscopic architecture, mesosuperstructured, planar heterojunction structure, and heterojunction-depleted in CsSnI₃ thin films based perovskite solar cells.^[120] They demonstrated that the heterojunction-depleted structure fits well to the lead-free perovskite solar cells. The work was started with the synthesis of an in-house prepared high quality CsSnI₃ feedstock (Figure 17A), which is not sensitive to the fabrication conditions with the formation of the undesirable Y-CsSnI₃ polymorph and the degradation product Cs₂SnI₆. Moreover, Sn vacancies with intrinsic low formation-energies in the CsSnI₃ structure can be avoided. The microstructures of CsSnI₃ thin films without annealing and with annealing at 100 to 300 °C were carefully investigated (Figure 17B). The coarsening of the grains with increasing annealing temperature is clearly observed. The device structure was systematically investigated by employing a mesoscopic architecture, mesosuperstructured, and planar heterojunction structure (Figure 17C); however, the performance was not satisfied (Figure 17D) due to the low crystallinity of the CsSnI₃ perovskite in the mesopores of the TiO₂ or Al₂O₃ scaffolds and, the nonideal solid-solid interfaces between the perovskite and the scaffold material, and the low-crystallinity impurities, such as

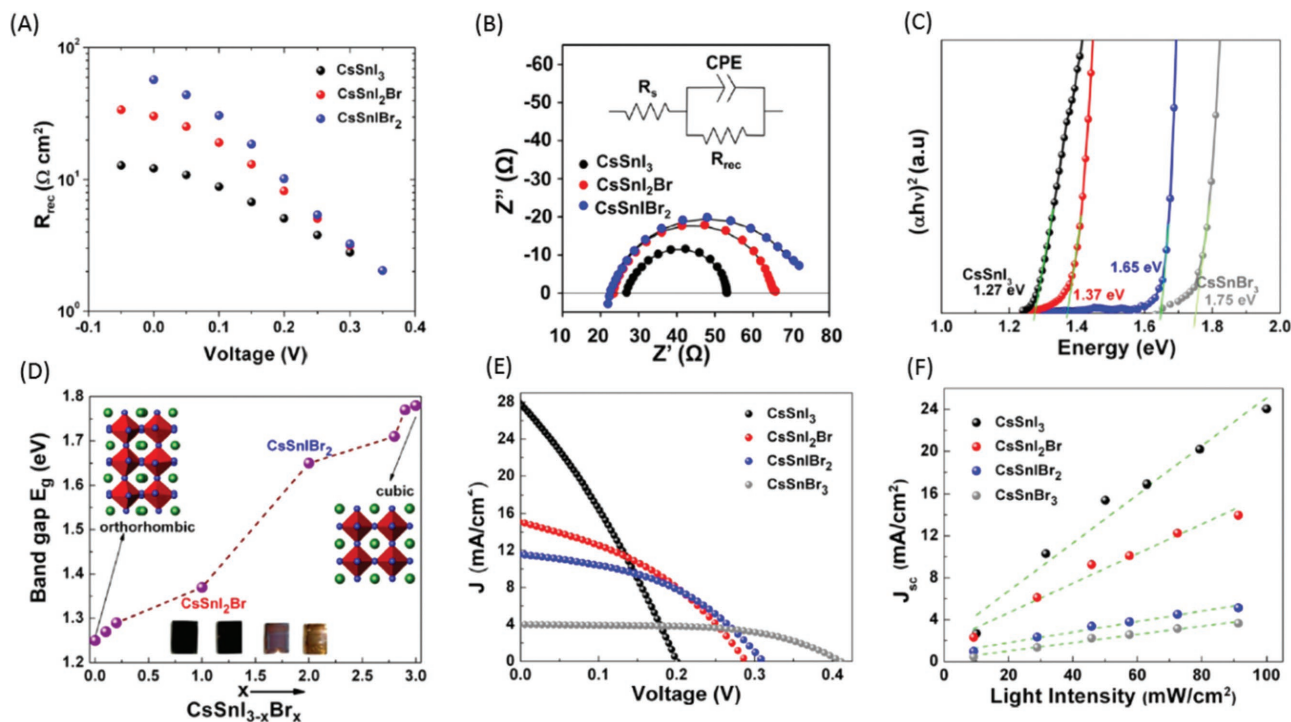


Figure 16. A) Recombination resistance against applied voltage, B) Nyquist plot for CsSnI₃ (Black), CsSnI₂Br (red), and CsSnIBr₂ (blue). C) Absorption pattern of CsSnI_{3-x}Br_x indicating light absorption onset blue shift from CsSnI₃ to CsSnBr₃. D) Tendency chart of CsSnI_{3-x}Br_x (x vary from 0 to 3.0). E) J–V curve of solar cell device. F) Contribution of Light intensity to J_{sc} for CsSnI₃ (Black), CsSnI₂Br (red), and CsSnIBr₂ (blue). Reproduced with permission.^[119] Copyright 2015, American Chemical Society.

Y-CsSnI₃ and Cs₂SnI₆, in the as-crystallized CsSnI₃ thin films upon mesoporous scaffolds. To overcome these issues, a hetero-junction-depleted structure was employed with energy-matched NiO_x as a hole transporting layer and PCBM as an electron

transporting material (Figure 17E). The best-performing PCE of 3.31% was achieved to date with a V_{oc} of 0.52 V, J_{sc} of 10.21 mA cm⁻², and FF of 0.625 (Figure 17F). The results indicated that the rational design of the device architecture and the

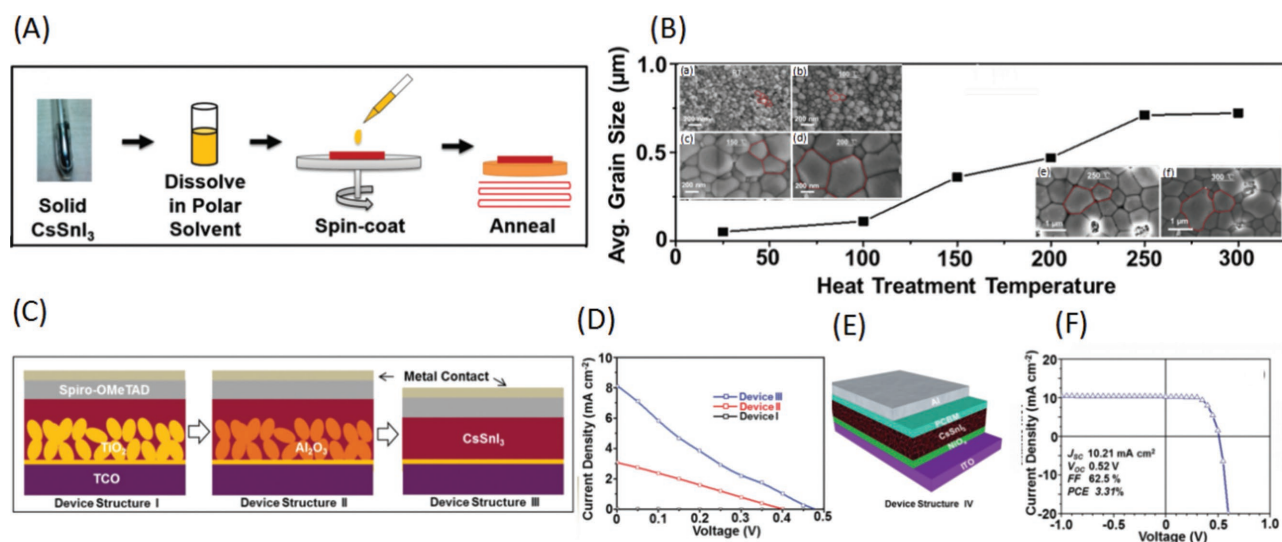


Figure 17. A) Schematic of one-step solution process of B- γ -CsSnI₃ films. B) Average grain size of B- γ -CsSnI₃ films with different annealing temperature varied from room temperature (RT) to 300 °C (inset shows corresponding SEM images of B- γ -CsSnI₃ films. a) RT, b) 100, c) 150, d) 200, e) 250 and f) 300 °C). C) Devices structure evolution of B- γ -CsSnI₃ PSCs. D) J–V curves obtained from Device I, Device II and Device III corresponding to (C). E) Planar inverted device structure of B- γ -CsSnI₃ PSCs with NiO_x and PCBM as HLM and ELM respectively. F) J–V curve obtained from B- γ -CsSnI₃ planar inverted champion device which shows best to-date parameter compared with <1% PCE previously reported. Reproduced with permission.^[120] Copyright 2016, Wiley-VCH Verlag GmbH & Co. KGaA, Weinheim.

lead-free perovskite microstructures are important for the further development of high-performance lead-free PSCs.

Unlike CsSnI₃ perovskite, which have Sn in the 2+ oxidation state and must be handled in an inert atmosphere when fabricating solar cells, Cs₂SnI₆ perovskites with a Sn 4+ oxidation state are stable in air and moisture.^[109,121] The missing half of the Sn in the octahedral structure compared to CsSnI₃ contributes to the formation of octahedral dispersive [SnI₆]²⁻ molecular and to the cubic space group resulting in a 0-D structure.^[85] The band gap of 1.3 eV was obtained by Chang et al. at room temperature, which is lower than the thermal-evaporated film with 1.6 eV.^[109,121] The difference may be attributed to the different preparation of the films. Since solution-processed films showed different morphology than thermal-evaporation films.^[23] Even though in the same method, e.g., solution-processed, one-step and two-step methods gave different morphology and thickness. The morphology and thickness could significantly influence the absorption and thus the band gap.^[15] However, Cs₂SnI₆ cannot be used as an active layer in real perovskite solar cell. The pristine Cs₂SnI₆ behaves as an n-type semiconductor with a high electron mobility of 310 cm²/V·s independently confirmed by room-temperature Hall effect measurements and the Seebeck coefficient.^[126] While doping Cs₂SnI₆ with Sn²⁺ yields properties of p-type semiconductor confirmed by the Seebeck coefficient with the hole mobility of 42 cm²/V·s. This behavior provides solid evidence of the ambipolar nature of Cs₂SnI₆.

3.2. Ge-based Perovskite Solar Cell

Ge²⁺ has smaller ionic radii than Sn²⁺ and Pb²⁺, but has similar outer ns² electrons (4s²) similar to Sn²⁺ (5s²) and Pb²⁺ (6s²). Previous reports have shown that the outer ns² electrons

structure of metal ions with low ionization energy is helpful to obtain better optical absorption and carrier diffusion in ABX₃ structures.^[62] AGeI₃ (A = Cs, CH₃NH₃ or CH₂(NH₂)₂) are demonstrated to be thermodynamic stable up to 150 °C which is relatively promising for photovoltaic applications. With large halogen iodide cooperation, large polarizability of the germanium iodide (GeI₂) was obtained due to the mismatch between Ge and I, indicating Ge analogues show a remarkable tendency to crystallize in a polar space group, unlike their congeners. Perhaps, drawbacks of Ge-based perovskites are still mainly the high oxidation tendency and poor film morphology like Sn-based perovskites.

Theoretical calculations made by Mathews et al. have shown that Ge can be an alternative replacement for lead-free perovskite applications.^[122] Experimentally, CsGeI₃ with an optical bandgap of 1.63 eV is close to the conventional lead halide perovskite of ≈1.5 eV compared to the MAGEI₃ of 2.0 eV and FAGEI₃ of 2.35 eV (Figure 18A), which give rhombohedral crystal structures at room temperature. Interestingly, the bandgaps are increased with increasing the radii of A cations, which is inverse to the case of lead-based perovskites. The devices based on three kinds of Ge material were fabricated via a mesoporous TiO₂ structure (Figure 18B) using hypophosphorous acid to improve the dissolution of the Ge-based perovskite precursor in organic solvent. MAGEI₃ and CsGeI₃ show photovoltaic properties with J_{sc} of 4.0 and 5.7 mA cm⁻² and PCE of 0.11 and 0.2%, respectively (Figure 18C). Both of the MAGEI₃ and CsGeI₃ films show nearly full-coverage morphology as observed from the SEM image (Figure 18D and E) corresponding to their device performance. However, FAGEI₃ gave a relatively poor film morphology resulting in no photocurrent observed from its samples. It is worth noting that Ge²⁺ in perovskite is easily oxidized to Ge⁴⁺ similar to Sn²⁺ in CsSnI₃

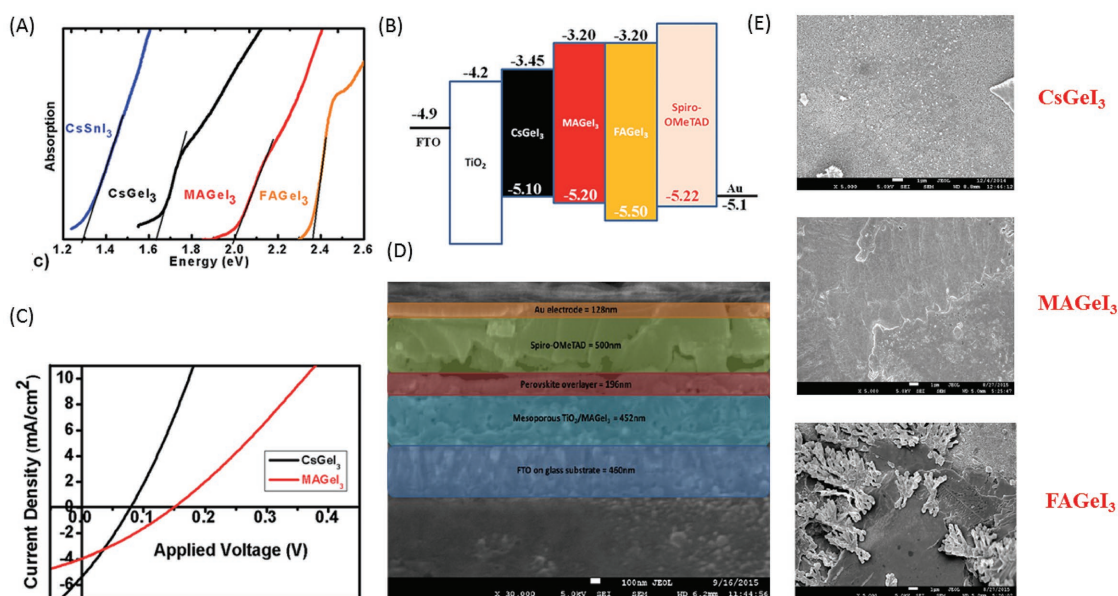


Figure 18. A) Tauc plot for CsGeI₃, MAGEI₃, and FAGEI₃ showing optical bandgaps of 1.63, 2.0, and 2.35 eV respectively. B) Energy level pattern for CsGeI₃, MAGEI₃, and FAGEI₃ based PSCs. C) J–V curves for CsGeI₃ and MAGEI₃ solar cells showing PCE of 0.11 and 0.20%, respectively. D) Cross-section SEM image for MAGEI₃ PSCs. E) SEM images for CsGeI₃, MAGEI₃, and FAGEI₃ films both deposited on the compact and mesoporous TiO₂ substrates. Reproduced with permission.^[122] Copyright 2015, The Royal Society of Chemistry.

perovskite, contributing to a relatively low V_{oc} of 150 and 74 mV for $MAGeI_3$ and $CsGeI_3$.

Moreover, using $CsGeI_3$ (1) as the prototype compound, a series of Ge-based perovskites based on the trigonal pyramidal $[GeI_3]^-$ building block have been synthesized through tuning A-cations by Kanatzidis et al.,^[123] e.g., methylammonium, $MAGeI_3$ (2), formamidinium, $FAGeI_3$ (3), acetamidinium, $CH_3C(NH_2)_2GeI_3$ (4), guanidinium, $C(NH_2)_3GeI_3$ (5), trimethylammonium, $(CH_3)_3NHGeI_3$ (6), and isopropylammonium, $(CH_3)_2C(H)NH_3GeI_3$ (7) analogues. The incorporation of the small polar organic ammonium replacing Cs^+ has a dramatic effect on the electronic structure of the perovskites as the cation size increases. The crystal structures of the compounds show that formation of a 3D perovskite structure is obtained for the 1–4 compounds with direct band gaps of 1.6 (1), 1.9 (2), 2.2 (3), and 2.5 eV (4) while the 5–7 compounds give 1D infinite chains with indirect band gaps of 2.7 (5), 2.5 (6), and 2.8 eV (7). They also demonstrated that all Ge-based perovskites exhibit a large second harmonic generation (SHG) response resulting from sp-hybrid orbitals of Ge and I. The SHG showed that $MAGeI_3$ and $FAGeI_3$ have a larger response than $CsGeI_3$, indicating high valence-band states of both $MAGeI_3$ and $FAGeI_3$. In addition, $CsGeI_3$, $MAGeI_3$, $FAGeI_3$, and $CH_3C(NH_2)_2GeI_3$ could be developed as non-linear optics materials in the visible and near-IR regions due to phase-matchability and high SHG conversion efficiencies. This work opens a path for a more general application by substituting small organic ammonium cation with other polar compounds to tune the band gap and SHG conversion efficiency.

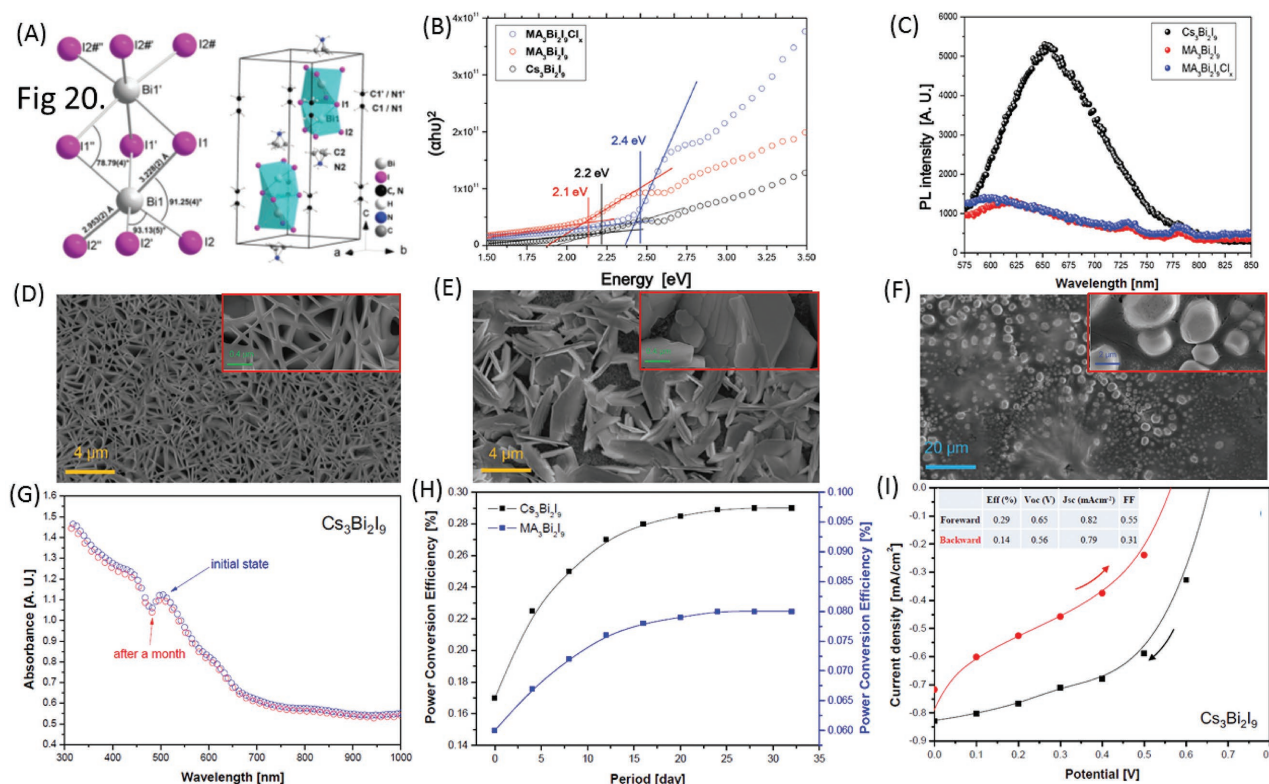
Therefore, there is still great room for Sn and Ge-based perovskites in terms of efficiency and stability. First, the rational design of the device architecture is important for charge extraction and balanced transport. Planar heterojunction structure has been demonstrated as suitable for Sn-based perovskite solar cells.^[120] Second, Sn and Ge-based perovskites exhibit significantly different energy structures from that of Pb-based perovskites. Accordingly, the corresponding ETL and HTL must be redesigned or selected to facilitate charge extraction. Thirdly, stabilizing Sn^{2+} and Ge^{2+} in Sn and Ge-based perovskites needs to be further investigated for not only improvement of performance but also long-term outdoor applications. Finally, due to the fast crystallization of Sn-based perovskites, exploring new fabrication methods controlling perovskite crystallization and microstructures should not be ruled out.

3.3. Bi and Sb-based Perovskite Solar Cells

The $6s^26p^0$ electronic configuration of Pb^{2+} allows for the filled 6s orbital to mix with the iodide 5p orbitals in the valence band while the vacant lead 6p orbitals form the conduction band,^[124] which contribute to the material's shallow defect states and long carrier lifetimes. Moreover, the high p-orbital-based density of states near the band-edges provide for the material's strong absorption.^[125] Only Tl^+ , Pb^{2+} , and Bi^{3+} have the same $6s^26p^0$ electronic configuration, out of which only Bi has low toxicity. Furthermore, being adjacent cations in the periodic table, the Bi^{3+} and Pb^{2+} have very similar ionic radii, which may lead to easy incorporation into the perovskite lattice.^[126] Bi^{3+} is also a

promising stable metal ion compared to Sn^{2+} and Ge^{2+} , which are easily degraded under atmosphere. In fact, Bi has been used for decades as a nontoxic replacement for Pb in areas ranging from organic synthesis to ammunition materials.^[127] Recently, Bi^{3+} has been used as a dopant to dope PbS in both thin films^[128] and quantum dots,^[129] converting them from p-type to n-type semiconductors. More importantly, a controlled incorporation of Bi^{3+} into the $MAPbBr_3$ and $MAPbI_3$ lattice has been successfully achieved, which leads to bandgap tuning (≈ 300 meV), a 10^4 fold enhancement in electrical conductivity, and a change in the sign of the majority charge carriers from positive to negative. Previous reports have found that the Bi^{3+} forms regular chains built of nearly regular octahedra with halide anions.^[130,131] Accordingly, Bi^{3+} could be a great candidate for lead-free PSCs.

Ternary bismuth halides have emerged as interesting functional materials closely related Pb halide perovskites for photovoltaic applications, especially given the significantly reduced toxicity of Bi. A few investigations of crystal structures, optical, dielectric, and quantum physical properties on Bi-based perovskite films, $Cs_3Bi_2I_9$ or $MA_3Bi_2I_9$, have been actually done previously; however, no report was made on solar cells application.^[132–135] Johansson et al. reported and successfully fabricated $A_3Bi_2I_9$ ($A = MA$ or Cs) perovskites and first integrated them into photovoltaic devices with the structure of $MA_3Bi_2I_9$, $Cs_3Bi_2I_9$, and $MA_3Bi_2I_9Cl_x$, respectively.^[136] Since the substitutions of Bi^{3+} are heterovalent, $A_3Bi_2I_9$ perovskites involved 1/3 bi-deficient layered perovskite with bi-octahedral $(Bi_2I_9)^{3-}$ clusters that are surrounded by A^+ (Cs^+ or MA^+). The single crystal structure of $MA_3Bi_2I_9$ perovskite was systematically investigated for the first time by Kaskel et al., where every two Bi^{3+} were combined with each other via three equivalent symmetrical I^- and every three terminal I^- were situated on the other sides of the mirror planes (Figure 19A).^[137] The absorption coefficients were estimated to around 1×10^5 cm^{-1} at 450 nm for the different bismuth perovskites with optical bandgaps estimated to be around 2.1, 2.2, and 2.4 eV for $MA_3Bi_2I_9$, $Cs_3Bi_2I_9$, and $MA_3Bi_2I_9Cl_x$, respectively (Figure 19B). Accordingly, the exciton binding energies are estimated and calculated to be around 70–300 meV from the optical band gaps and the peaks in the PL spectra (Figure 19C) for the different perovskites, which is significantly higher compared to the exciton binding energy in the lead halide perovskites (25–50 meV).^[138,139] The components have significant effect on the bismuth perovskite morphology. The $MA_3Bi_2I_9$ perovskite gives an interconnected thin layer (around 50 nm thick) structure (Figure 19D) while $Cs_3Bi_2I_9$ (Figure 19E) shows hexagonal thin sheets. It is worth noting that $BiCl_3$ appears in the $MA_3Bi_2I_9Cl_x$ sample when chlorine was doped into the Bi-based perovskite which may result in its high bandgap and exciton leading to imparities of film morphology (Figure 19F). The champion photovoltaic devices of the three kind of perovskites were obtained with J_{sc} of 2.15 $mA\ cm^{-1}$, V_{oc} of 0.85 V, FF of 0.60, and PCE of 1.09% from the $Cs_3Bi_2I_9$ -based device. Therefore, interface engineering is needed to enhance the performance of the device through morphology controlling to promote the low PCE of Bi-based PSCs. The Bi-based PSCs show much stability, with the absorption exhibiting few changes after one month in the condition of dry air (moisture below 10%) and dark atmosphere (Figure 19G),



and the PCE even increased during the first 24 h after fabrication and maintained a stable value in the next days. It may be contributed from the fact that the Bi ion is stable at the +3 valance state in the PSCs (Figure 19H). However, the hysteresis may be a potential issue that arises changing from almost 0 initially to a much larger amount after one month (Figure 19I).

It can be seen that the device efficiency based on bismuth perovskites was much lower than lead based perovskites. It is unclear whether that is limited by the fabrication method, possible phase impurities, or sub-optimal contacts since the morphology of MA₃Bi₂I₉ still needs to be further improved. Very recently, phase-pure MA₃Bi₂I₉ was synthesized by solution-processing and vapor-assisted techniques by Buonassisi et al. (Figure 20A).^[140] The crystal structure, stability, and optoelectronic properties of MA₃Bi₂I₉ were systematically investigated. From the XRD pattern, the obtained thin film phase corresponds to the pure MA₃Bi₂I₉ phase as was confirmed by calculations (Figure 20B). They also found that MA₃Bi₂I₉ consists of Bi₂I₉³⁻ groups alternating with MA⁺ (Figure 20C and D), corresponding to previous report although using a different film deposit approach.^[142] The compact and layered morphology of MA₃Bi₂I₉ perovskites was confirmed by AFM and SEM, as shown in Figure 20E and F, which is suitable for solar cell applications. The air stability of MA₃Bi₂I₉ perovskite compared to MAPbI₃ by exposing both films to ambient air with around 61% relative humidity at room temperature was also

investigated. MAPbI₃ changed from brown to yellow after 5 d while MA₃Bi₂I₉ maintained the same visual appearance after 13 d (Figure 20G), demonstrating a stable photovoltaic absorber for MA₃Bi₂I₉ perovskites (Figure 20H). Moreover, vapor processed films gave longer PL decay times over 760 ps with the bulk lifetime possibly closer to 5.6 ns rather than solution processed method (Figure 20I). This work showed a strong motivation for MA₃Bi₂I₉ perovskite for solar absorbers and photovoltaic development in the point of view of great optoelectronics.

Moreover, all inorganic bismuth iodides perovskites A₃Bi₂I₉ (A = K, Rb, Cs) have been experimentally and computationally investigated by Lehner et al. From the calculated band structures, the band gaps of the layered K and Rb-based perovskites are direct while Cs₃Bi₂I₉ has an indirect gap. The optical band gaps and absolute highest occupied molecular orbital (HOMO) positions were determined by UV–Vis and by ultraviolet photoelectron spectroscopy (UPS), respectively, as shown in Figure 21A, B, and C.^[141] We can clearly see that the absorption edge is located at approximately 2 eV for all three ternary bismuth iodides, which corresponds to a previous report,^[136] while the binary exhibits a gap of about 1.8 eV. The deep HOMO energy requires hole transporting materials with deeper HOMO to maximize the V_{oc}. Recently, a layered perovskite-like architecture, (NH₄)₃Bi₂I₉, which is isostructural to hexagonal Rb₃Bi₂I₉, was also prepared from solution and the structure solved by single crystal X-ray diffraction, as shown in

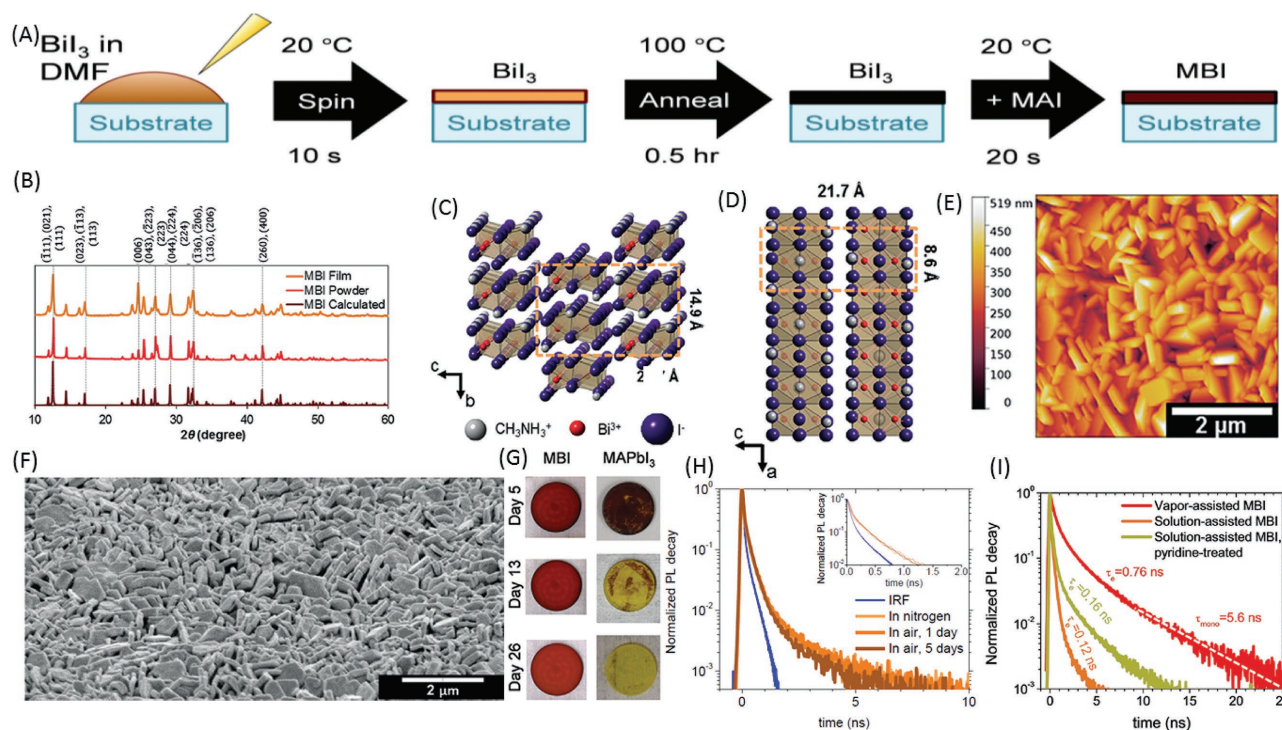


Figure 20. A) schematic diagram of $\text{MA}_3\text{Bi}_2\text{I}_9$ solution-assisted process. B) XRD pattern of $\text{MA}_3\text{Bi}_2\text{I}_9$ for different time. C) Crystal structure and D) 001 view of $\text{MA}_3\text{Bi}_2\text{I}_9$. E) AFM and F) SEM images of $\text{MA}_3\text{Bi}_2\text{I}_9$ thin films. G) Stability of $\text{MA}_3\text{Bi}_2\text{I}_9$ in air. H) PL decay pattern of $\text{MA}_3\text{Bi}_2\text{I}_9$ at different days in air. I) PL decay pattern of $\text{MA}_3\text{Bi}_2\text{I}_9$ with different processes. Reproduced with permission.^[140] Copyright 2016, Wiley-VCH Verlag GmbH & Co. KGaA, Weinheim.

Figure 21D.^[142] The band gap, which is estimated to be 2.04 eV (Figure 21E), is lower than that of MAPbBr_3 . The band gap is further reduced compared to larger K, Rb, Cs, and MA cations. This confirms the potential of $(\text{NH}_4)_3\text{Bi}_2\text{I}_9$ as an alternative to the lead-containing perovskites. Therefore, the size of the A cations needs to be small to obtain a narrow band gap for the $\text{A}_3\text{Bi}_2\text{I}_9$ perovskite.

Similar to bismuth, an antimony-based lead-free stacked layered perovskite derivative $\text{Cs}_3\text{Sb}_2\text{I}_9$ with large grain size over 1 μm (Figure 22A) and an optical band gap value of 2.05 eV (Figure 22B) has also been intensively investigated by Mitzi et al.^[143] A highly oriented $\text{Cs}_3\text{Sb}_2\text{I}_9$ thin film can be achieved by annealing the coevaporated film in SbI_3 vapor at 300 °C for 10 min, which was confirmed by XRD patterns (Figure 22C). Moreover, the well-crystallized thin films show only a very modest evolution of CsI impurity formation over the time scale of the experiment under high temperature (Figure 22D) while a MAPbI_3 thin film degrades more quickly as indicated by a strong PbI_2 impurity peak after 60 d of ambient air exposure (Figure 22E). The incorporation of $\text{Cs}_3\text{Sb}_2\text{I}_9$ into a solar cell yielded a PCE lower than <1% and the device exhibited hysteresis effect (Figure 22F), indicating the performance need further optimization.

3D materials are more favorable for photovoltaic applications than 2D materials in view of lower bandgap, smaller exciton banding energy, and longer exciton diffusion length. Sargent et al. therefore pursued a new approach to solution processed bismuth-based thin-film photovoltaic absorbers AgBi_2I_7 with a pure cubic structure, as shown in Figure 23A, B, and C,^[144]

which is prepared by spin-coating silver and bismuth precursors dissolved in *n*-butylamine and annealed under N_2 . The new material was presented by incorporation of monovalent silver cations into iodobismuthates instead of alkali metal cations. The surface morphologies of crystallized films became dense and uniform with increase annealing temperature from 90 to 150 °C (Figure 23D). When the temperature was increased to 150 °C, the pinhole-free film exhibited grains having sizes of 200–800 nm. The optical absorption spectra (Figure 23E) of Ag-Bi-I thin films was also identified and got better with an increase in the annealing temperature. The 150 °C annealed films show substantial absorption over the range of 350–750 nm with an E_g of 1.87 eV for AgBi_2I_7 assuming a direct band gap (Figure 23F). Finally, a J_{sc} of 3.30 mA cm^{-2} , V_{oc} of 0.56 V, FF of 67.41%, and PCE of 1.22% were obtained from the best solar cells (Figure 23G), which is the highest report to date.

In addition to +1 cation-based trivalent bismuth or antimony perovskites as representatives for lead-free perovskite in terms of toxicity and instability, +1 cation-based trivalent bismuth, e.g., dicationic alkyldiammonium bismuth halide perovskite HDABi_5 was also reported.^[145–147] However, as we see, the above intensively investigated trivalent bismuth or antimony perovskite gave lower dimensionalities and therefore wider band gaps than their 3D analogues. In order to maintain the 3D perovskite architecture, an alternative approach is to use a combination of a monovalent cation and a trivalent cation in an ordered B-site arrangement replacing Pb^{2+} to form a double perovskite structure of general formula $\text{A}^1\text{B}^1\text{B}^{\text{III}}\text{X}_6$. Hybrid binary metal double perovskite with Ag^+ and Bi^{3+} in

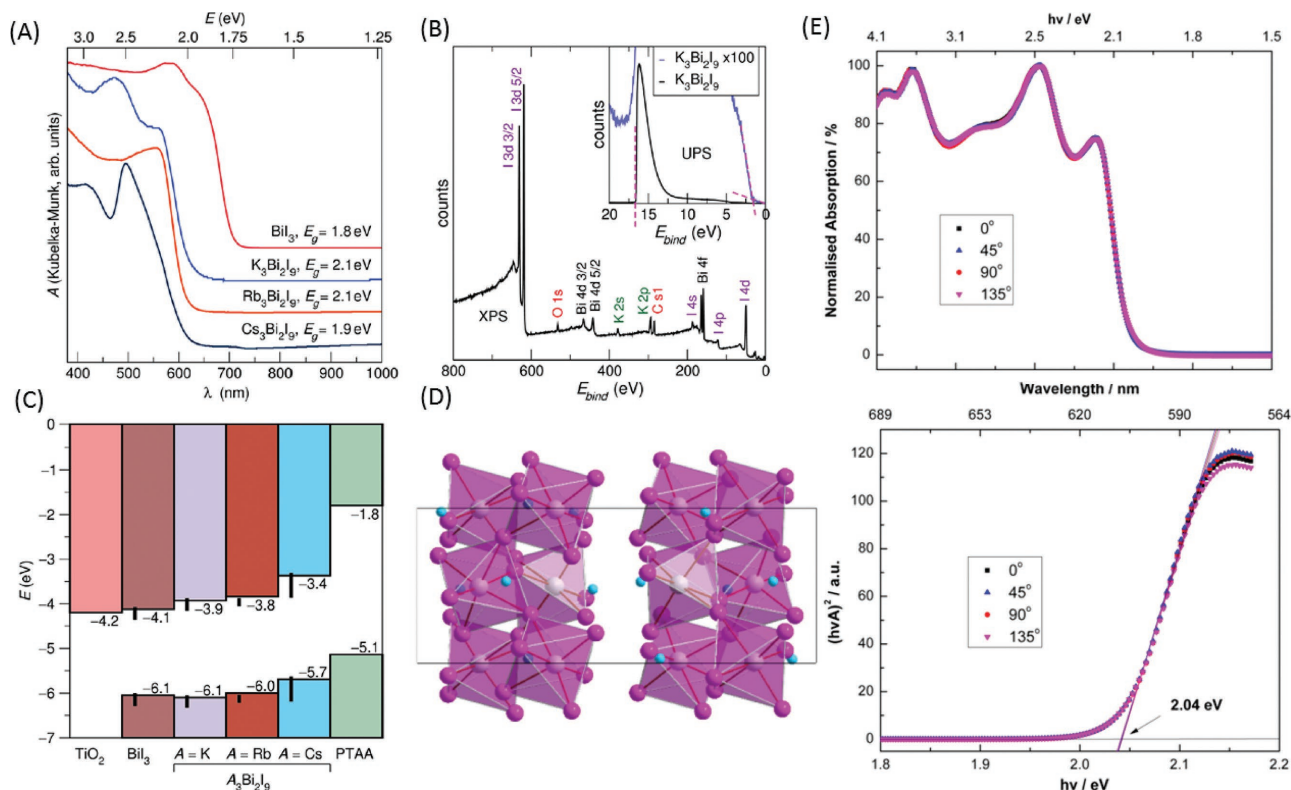


Figure 21. A) Diffuse reflection spectra of $A_3Bi_2I_9$ and BiI_3 powder sample, showing their bandgaps with Tauc plots. B) UPS and XPS spectra of $K_3Bi_2I_9$. C) Calculated energy levels of $A_3Bi_2I_9$ from DFT (PBE+SOC) theory, experimental energy levels of PTAA and the calculated HOMO energy level of TiO_2 . D) Crystal structure, E) Absorption spectrum and Tauc plot of $(NH_4)_3Bi_2I_9$. A–C) Reproduced with permission.^[141] Copyright 2015, American Chemical Society. D–E) Reproduced with permission.^[142] Copyright 2016, American Institute of Physics.

the B position also provide an alternative to realize the high stability lead-free PSCs where the Ag valance band of +1 and the Bi valance band of +3 both are stable states. The oxide double perovskites $A_2BB'O_6$ have actually been well explored and incorporate a wide variety of metals in various oxidation states.^[148] However, there are far fewer reports of halide double perovskites except $A_2Au^IAu^{III}X_6$ ($A = K, Rb, \text{ or } Cs; X = Cl, Br, \text{ or } I$),^[149] $Cs_2TI^ITl^{III}X_6$ ($X = F \text{ or } Cl$),^[150] and $Cs_2Ag^IAu^{III}Cl_6$.^[151] Karunadasa et al. for the first time reported $Cs_2AgBiBr_6$ double perovskite incorporating Bi^{3+} in a 3D perovskite framework (Figure 24A).^[152] A shallow absorption region beginning at 1.8 eV followed by a sharp increase in absorption near 2.1 eV was achieved in a $Cs_2AgBiBr_6$ double perovskite, corresponding to a recent report^[153] and demonstrating the suitability for photovoltaic applications from the point of view of optical absorption (Figure 24B). The perovskite showed the characteristics of an indirect bandgap semiconductor as confirmed by a Tauc plot, (inset of Figure 24B) estimating the indirect bandgap as 1.95 eV with an assisting phonon energy of 0.12 eV, which could be suitable for higher-bandgap absorbers in a tandem solar cell. In addition, the electron micrograph shows a promising grain-size distribution between 1–20 μm for a $Cs_2AgBiBr_6$ powder. (Figure 24C). Moreover, a long carriers recombination lifetime reaching 660 ns for $Cs_2AgBiBr_6$ comparing to 730 ns to 1 μs for $MAPbI_3$ makes $Cs_2AgBiBr_6$ another promising photovoltaic property (Figure 24D). From powder to single crystal, the PL lifetime of $Cs_2AgBiBr_6$ only undulates slightly which is

unusual even in an indirect bandgap material, indicating that $Cs_2AgBiBr_6$ has a higher tolerance parameter against defects, and original PL lifetime of this material can be confirmed. Most importantly, PXRD patterns of $Cs_2AgBiBr_6$ after moisture or light exposure showed no evidence of material decomposition although silver halides are notoriously light sensitive (Figure 24E) while $MAPbI_3$ and $MAPbBr_3$ heated at 60 °C for 72 h in air shows decomposition to PbI_2 and $PbBr_2$ (Figure 24F).

Almost at the same time, Woodward et al. also demonstrated $Cs_2AgBiBr_6$ and $Cs_2AgBiCl_6$ double perovskites with the structure of cubic lattice in the space group of $Fm\bar{3}m$ consisting of the $Ag(Br_6)Cl_6^{5-}$ and $Bi(Br_6)Cl_6^{3-}$ cubic octahedra structure confirmed by the X-Ray powder diffraction (XRPD) patterns (Figure 25A and B).^[154] Bandgaps 2.77 eV for $Cs_2AgBiCl_6$ and 2.19 eV for $Cs_2AgBiBr_6$ were obtained by UV–Vis diffuse reflectance spectra (Figure 25C and D), which corresponds to a previous report for $Cs_2AgBiBr_6$ (1.95 eV)^[150] and are both a little lower than the analogous conventional perovskite $MAPbCl_3$ of 3.00 eV and $MAPbBr_3$ of 2.26 eV, respectively. This inferred again that $Cs_2AgBiBr_6$ double perovskites are suitable for tandem solar cells as higher-bandgap absorbers combined with Si as another absorber. The stability of the two double perovskites was also obtained, as shown in Figure 25E and F, in which the reflectance spectrum for $Cs_2AgBiCl_6$ remains and no apparent change was detected in the XRPD patterns (Figure 25G) of $Cs_2AgBiCl_6$. The reflectance spectrum for $Cs_2AgBiBr_6$; however, changes dramatically after two weeks

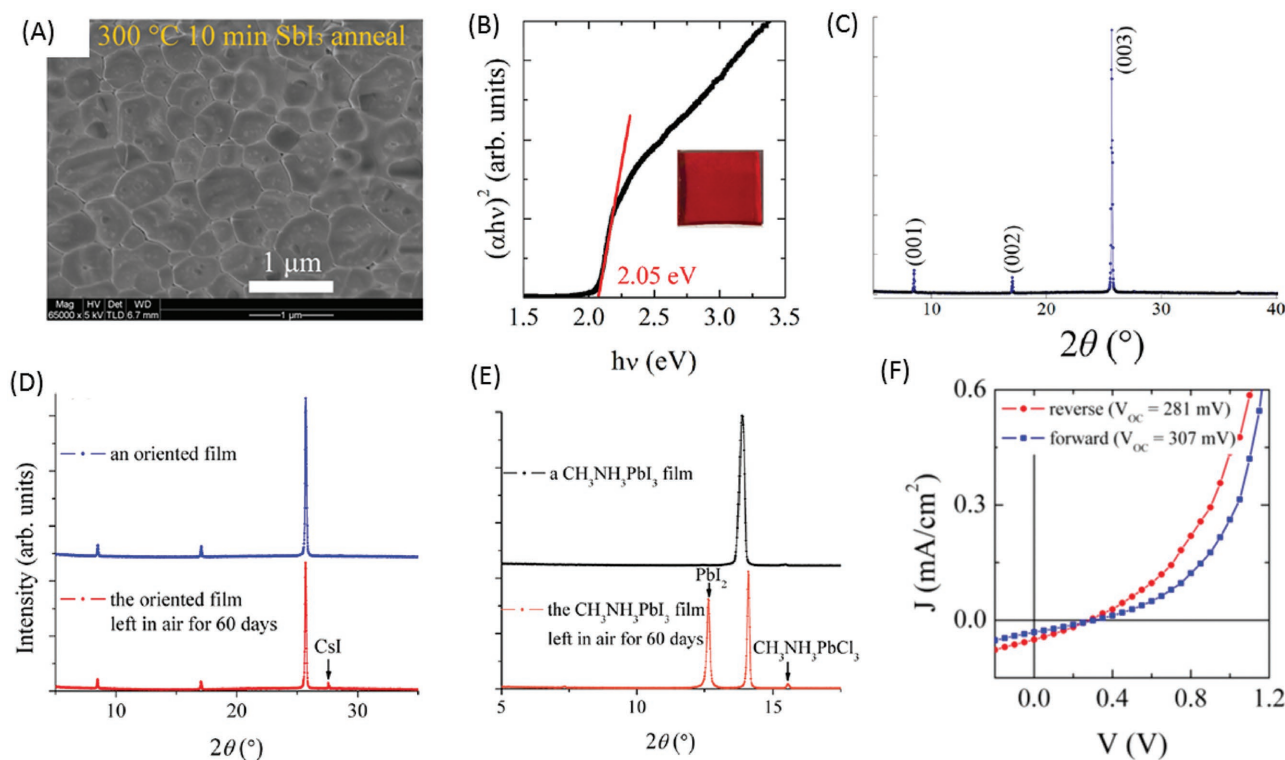


Figure 22. A) SEM image of $\text{Cs}_3\text{Sb}_2\text{I}_9$ thin film, deposited via coevaporation of CsI and SbI_3 followed by annealing at $300\text{ }^\circ\text{C}$ for 10 min in SbI_3 vapor atmosphere. B). Bandgap of layered $\text{Cs}_3\text{Sb}_2\text{I}_9$. C) PXRD pattern of $\text{Cs}_3\text{Sb}_2\text{I}_9$ via coevaporation, followed by annealing at $300\text{ }^\circ\text{C}$ for 10 min in SbI_3 vapor atmosphere. D) Evolution of CsI peak for c-axis oriented $\text{Cs}_3\text{Sb}_2\text{I}_9$ thin film stored in air for 60 d. E) Decomposition of MAPbI_3 thin film stored in air for 60 d. F) Hysteresis effect of layered $\text{Cs}_3\text{Sb}_2\text{I}_9$ PSCs with forward to reverse and reverse to forward directions. Reproduced with permission.^[143] Copyright 2015, American Chemical Society.

exposure to light and ambient air, accompanied by the appearance of unidentified phases in the XRPD (Figure 25H). These observations clearly show that the $\text{Cs}_2\text{AgBiBr}_6$ double perovskite phase could be degraded over time when simultaneously exposed to light and moisture but could be stable in only light or moisture exposure.

Snaith et al. reported the entire family of pnictogen noble-metal double-halide perovskites based on a $\text{A}_2\text{BB}'\text{X}_6$ structure, where $\text{B}' = \text{Sb}, \text{Bi}$ and $\text{B} = \text{Cu}, \text{Ag}, \text{Au}$ from computational screening.^[155] The electronic properties of these hypothetical compounds were investigated from first-principles using density functional theory in the local density approximation, as shown in Figure 26A, B, C and D. They found that all band gaps are below 2.7 eV with indirect characteristics and reduce with an increase to the radius of halogen or pnictogen. Moreover, all double perovskite exhibit small carrier effective masses between 0.1 and 0.4 m_e , which is very close to those calculated for MAPbI_3 within the same level of theory.^[156] Furthermore, they successfully synthesize the double perovskite $\text{Cs}_2\text{AgBiCl}_6$ with an indirect optical band gap in the range of 2.3 to 2.5 eV (Figure 26E), consistent with its calculated band structure (Figure 26F) and broad PL peak observed between 480 and 650 nm with the maximum at ≈ 575 nm (Figure 26G). Furthermore, $\text{Cs}_2\text{AgBiCl}_6$ gave the time-resolved photoluminescence decay with a double exponential giving a fast component lifetime of 15 ns and a slow component lifetime of 100 ns (Figure 26H). Regarding to cost; however, alkali-metal based

double-halide perovskites may be an alternative to noble-metal based double-halide perovskites.^[157]

As seen, ABi_2I_9 ($\text{A} = \text{Cs}, \text{MA}, \text{and FA}$) based perovskites have been intensively investigated; however, the efficiency is still limited. First, the Bi-based perovskite morphology still has large room for improvement by exploring new approaches for film fabrication. Second, the bandgap of Bi-based perovskites is higher than Pb-based perovskites. Doping could be a useful strategy to reduce the bandgap and thus get higher photocurrent. Finally, Bi-based perovskites with 3D structure ($\text{A}'_2\text{B}^{\text{I}}\text{B}^{\text{II}}\text{X}_6$) were obtained in the form of single crystals or the study remains at the calculation stage. Achieving 3D Bi-based perovskite films with uniform crystals and full coverage of substrate may help to accelerate the development of Bi-based perovskites.

3.4. Transition Metal Ions for Lead-free Perovskite Solar Cells

$\text{Sn}, \text{Ge}, \text{Bi}$ and Sb are represented to be alternatives for Pb in perovskite. However, cost is still the primary limitation for further lead-free perovskite advances. Naturally, transition metal ions (e.g., $\text{Cu}^{2+}, \text{Fe}^{2+}, \text{Zn}^{2+}$) might act as potential roles in the big lead-free perovskite family. New transition-metal perovskites can be synthesized via a variety of routes to manage photovoltaic properties. As a result of smaller ionic radii of transition metal ions, 3D structure is not able to produce and then

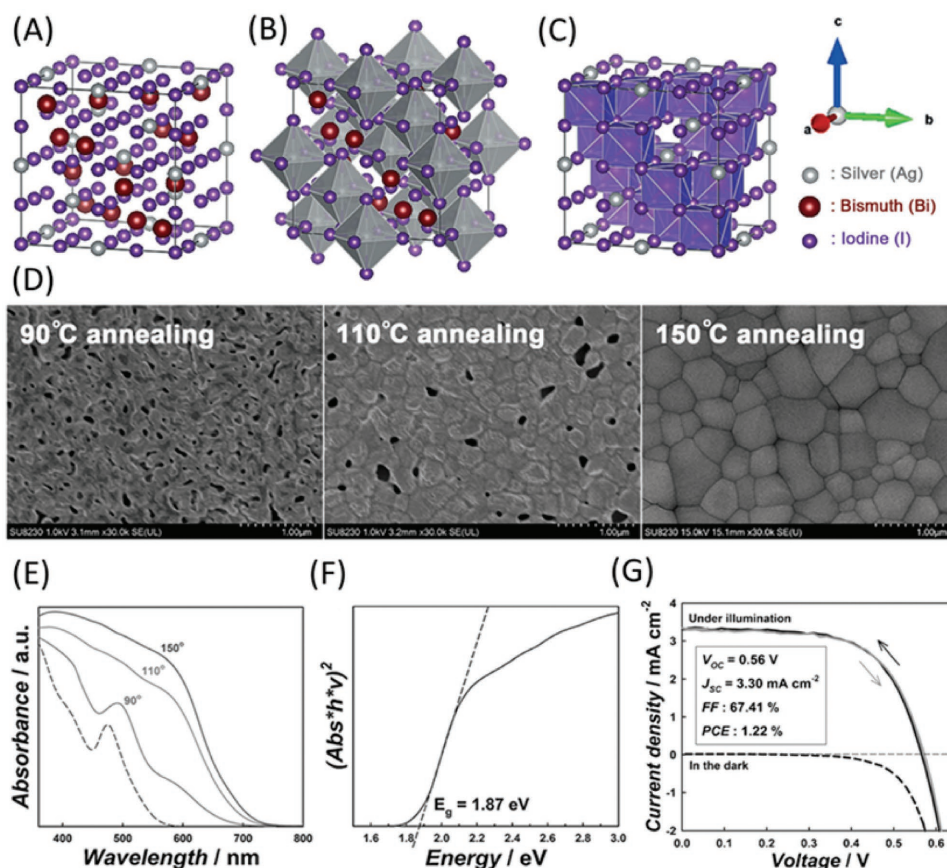


Figure 23. A) The cubic structure of AgBi_2I_7 (space group $Fd\bar{3}m$, $a = b = c = 12.223 \text{ \AA}$) with the joint population of a single position by silver, bismuth, and iodide. The unit cell of AgBi_2I_7 is expressed with B) six-coordinated silver-iodide octahedron sites and C) eight-coordinated bismuth-iodide hexahedron sites. D) Top-view SEM images of solution-processed AgBi_2I_7 thin-films as a function of annealing temperature. E) UV/Vis spectra of AgBi_2I_7 thin-films as a function of annealing temperature. F) Tauc plot of AgBi_2I_7 . G) J - V curves in the dark and illumination under 100 mW cm^{-2} AM 1.5G. Reproduced with permission.^[144] Copyright 2016, Wiley-VCH.

convert into a 2D layered structure (e.g., 3D structure is cut along $\langle 100 \rangle$, $\langle 110 \rangle$ and $\langle 111 \rangle$ orientations and piled up layer-by-layer to form the 2D structure) like K_2NiF_4 or $\text{La}_{2-x}\text{Ba}_x\text{CuO}_4$. Long-chain cations and incorporation of mass metal atoms in these 2D structures allow compounds to form a wildly tunable structure, due to relaxed geometrical constrains. In transition metals, Cu^{2+} can be promising as it is stable in its 2+ oxidation state in atmosphere, earth-abundant, cost-effective and near-infrared absorption obtained from its compounds.

Cortecchia et al. first introduced the Cu-based halide perovskite as light harvester with the 2D crystal structure of $\text{MA}_2\text{CuCl}_x\text{Br}_{4-x}$ ^[158] in which the Cl^- play an essential role to realize high stability. Cu^{2+} play a passive role that can be reduced to Cu^+ providing higher density of trap. $\text{MA}_2\text{CuCl}_x\text{Br}_{4-x}$ exhibited promising light harvesting (Figure 27A, B) with the onset extending to near infrared in spite of the limitation of low absorption coefficient and heavy-mass holes. The associated band gap can be tunable by increasing the Br content from 2.48 eV for MA_2CuCl_4 to 1.80 eV for $\text{MA}_2\text{CuCl}_{0.5}\text{Br}_{3.5}$. Their powder color ranges from yellow, red, and dark brown with increasing Br/Cl ratio (Figure 27C). With a simple one-step method using DMSO as solvent to dissolve the mixture precursors of MABr, MA₂Cl, CuCl_2 , and CuBr_2 at different

ratios, the $\text{MA}_2\text{CuCl}_x\text{Br}_{4-x}$ active layer was spun coated onto the ITO/PEDOT:PSS substrate to fabricate the planar heterojunction devices (Figure 27D) or onto the FTO/mesoporous TiO_2 substrate to fabricate mesoporous devices that achieve a PCE of 0.017% (Figure 27E) with extremely low J_{sc} and V_{oc} of $216 \mu\text{A cm}^{-2}$ and 256 mV, respectively. The higher PCE obtained from the mesoporous structure compared with that obtained from the planar heterojunction (PHJ) structure is because the mesoporous TiO_2 can disrupt the 2D structure of $\text{MA}_2\text{CuCl}_x\text{Br}_{4-x}$ perovskite leading to the charge extraction and perpendicular charge transport. However, the low absorption coefficient and heavy-mass hole still limit the performance at the same time. This work provides guidelines for future optimization and investigation of lead-free perovskites based on transition metal ions.

Cu^{2+} is particularly interesting for lead-free perovskites due to the stable oxidation state and large absorption coefficient in Cu-based compounds in the visible region. However, it still has great challenges to overcome to achieve transition metal-based lead-free perovskite solar cells. Tremendous work needs to be done, such as lowering the bandgap, improving charge transport, enhancing exciton diffusion length, designing device structure, and exploring new fabrication methods. Appropriate

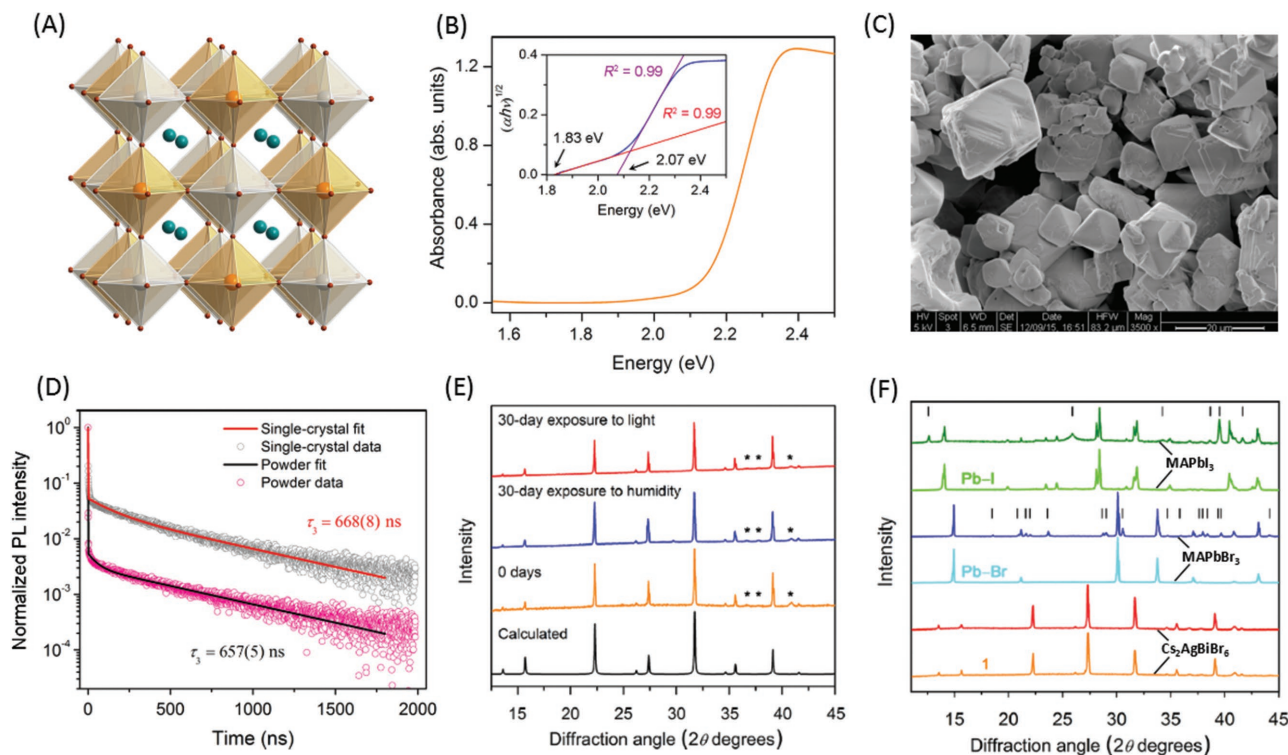


Figure 24. A) Crystal structure of $\text{Cs}_2\text{AgBiBr}_6$ (cyan for Cs, orange for Bi, gray for Ag and brown for Br). B) Absorption spectrum for $\text{Cs}_2\text{AgBiBr}_6$. Inset: Tauc plot showing optical bandgap of 1.95 eV implying a high energy phonon mode within the absorption. C) SEM image for $\text{Cs}_2\text{AgBiBr}_6$ with a grain size between 1–2 μm . D) Time-resolved PL decay for single crystal and powder $\text{Cs}_2\text{AgBiBr}_6$ in fit and data investigating powder sample have a shorter lifetime compared with the single crystal that indicate powder sample has more defects and surface states than single crystal. E) XRD patterns for measurements of $\text{Cs}_2\text{AgBiBr}_6$ samples stability under light and in humidity respectively for 30 d. F) XRD patterns of $\text{Cs}_2\text{AgBiBr}_6$, MAPbBr_3 , and MAPbI_3 before (orange, turquoise and light green) and after 72 h at 100 $^\circ\text{C}$ (red, blue, and dark green). Reproduced with permission.^[152] Copyright 2016, American Chemical Society.

molecular design is also necessary to improve the material's properties and solar cell performance.

4. Conclusion and Outlook

Here, we have critically reviewed recent advances of organic–inorganic hybrid environment-friendly lead-free PSCs experimentally and theoretically in order to achieve a better fundamental understanding of optoelectronics associated with lead-free perovskites. The conventional lead-based perovskite APbX_3 suffers from a high content of the toxic, polluting, and bioaccumulative lead, which may eventually hamper the large-scale implementation of this technology. This has spurred on the search for lead-free materials with similar optoelectronic properties. With theoretical calculations and experimental characterizations, a series of +2, +3 ions, e.g., Sn^{2+} , Bi^{3+} , Mg^{2+} , Ge^{2+} , Sb^{3+} , Cu^{2+} , in the ABX_3 structure can replace Pb^{2+} completely to form lead-free perovskites. Recent first principles calculations are catching up with intensive experimental investigations on PSCs. Theoretical simulations have made important contributions to understanding the fundamental physics behind the efficiency, stability, and carrier transport properties of inorganic–organic hybrid PSCs. Moreover, these theoretical works provided guidance on discovering and designing new, non-toxic, better performing solar absorption materials.

Several lead-free perovskites have been identified as potential substitutes for MAPbI_3 with MAGeI_3 , MAMgI_3 , $\text{MATl}_{0.5}\text{Bi}_{0.5}\text{I}_3$, MABiSI_2 , and MABiSeI_2 . Theoretical research on cation/anion alloyed solid solution perovskites and hybrid antimony sulfides significantly widens the selection pool of elements and structures for the design of environmentally-friendly and high-performance solar cell materials.

Recent experimental characterizations on Sn-based perovskite showed outstanding absorption with onset reaching 1000 nm and have reached a PCE of 6%, indicating that Sn^{2+} may become the most promising candidate. However, Sn^{2+} has a potential issue that it is rapidly oxidized to Sn^{4+} ruining the perovskite structure in air, which is considered as a bottleneck limiting the development of Sn-based PSCs. The same issue was found in Ge-based perovskites and the related device performance is highly limited. Bi-based perovskite was also intensively studied since Bi^{3+} has the same $6s^2$ lone-pair electron and similar ion radii with Pb^{2+} , which lead to similarities in chemical behavior and little distortion in structure. Moreover, Bi is dramatically stable at +3 valance state in atmosphere compared to Sn^{2+} . Unfortunately, the initial PCE of $\approx 0.1\%$ of Bi-based $\text{Cs}_3\text{Bi}_2\text{I}_9$ PSCs still needs further optimization in terms of film morphology, fabrication method, and device engineering. In addition, halide double perovskites $\text{A}_2\text{BB}'\text{X}_6$ provide a more accommodating platform for substitutions, where $\text{B} = \text{Cu}, \text{Ag}, \text{Au}$ and $\text{B}' = \text{Sb}, \text{Bi}$. Examples of double perovskite, $\text{Cs}_2\text{AgBiBr}_6$, shows

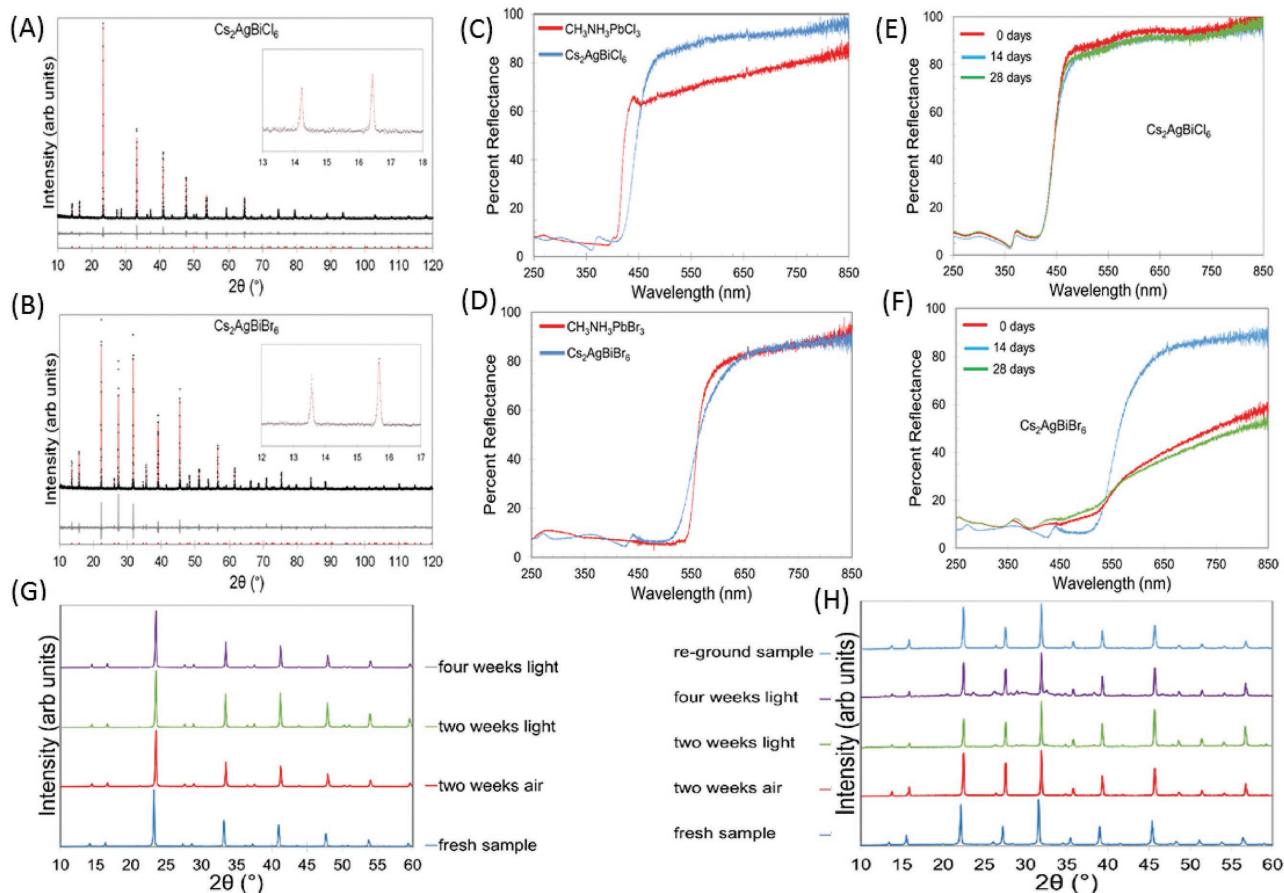


Figure 25. XRPD experimental patterns and calculated fits of A) $\text{Cs}_2\text{AgBiCl}_6$ and B) $\text{Cs}_2\text{AgBiBr}_6$. Diffuse reflectance spectrums of C) $\text{Cs}_2\text{AgBiCl}_6$ and MAPbCl_3 and D) $\text{Cs}_2\text{AgBiBr}_6$ and MAPbBr_3 . UV-Vis diffuse reflectance spectrum of E) $\text{Cs}_2\text{AgBiCl}_6$ and F) $\text{Cs}_2\text{AgBiBr}_6$. XRPD patterns of G) $\text{Cs}_2\text{AgBiCl}_6$ and H) $\text{Cs}_2\text{AgBiBr}_6$ at different times exposed to sunlight in air. Reproduced with permission.^[154] Copyright 2016, American Chemical Society.

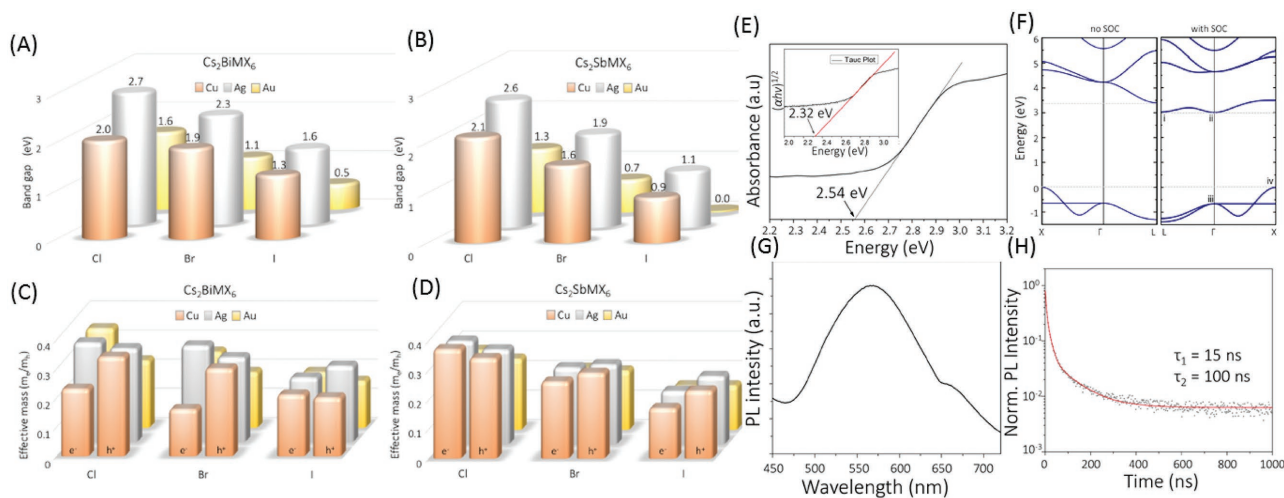


Figure 26. A) Calculated bandgap and C) effective mass of Cs_2BiMX_6 . B) Calculated bandgap and D) effective mass of Cs_2SbMX_6 . E) Absorption spectrum of $\text{Cs}_2\text{BiAgCl}_6$ with Tuac plot inset. F) Band structure of $\text{Cs}_2\text{BiAgCl}_6$ calculated with (right) and without (left) spin-orbit coupling (SOC). G) Steady-state PL spectrum of $\text{Cs}_2\text{BiAgCl}_6$ on glass. H) Time resolved PL decay spectrum of $\text{Cs}_2\text{BiAgCl}_6$ on glass. Reproduced with permission.^[155] Copyright 2016, American Chemical Society.

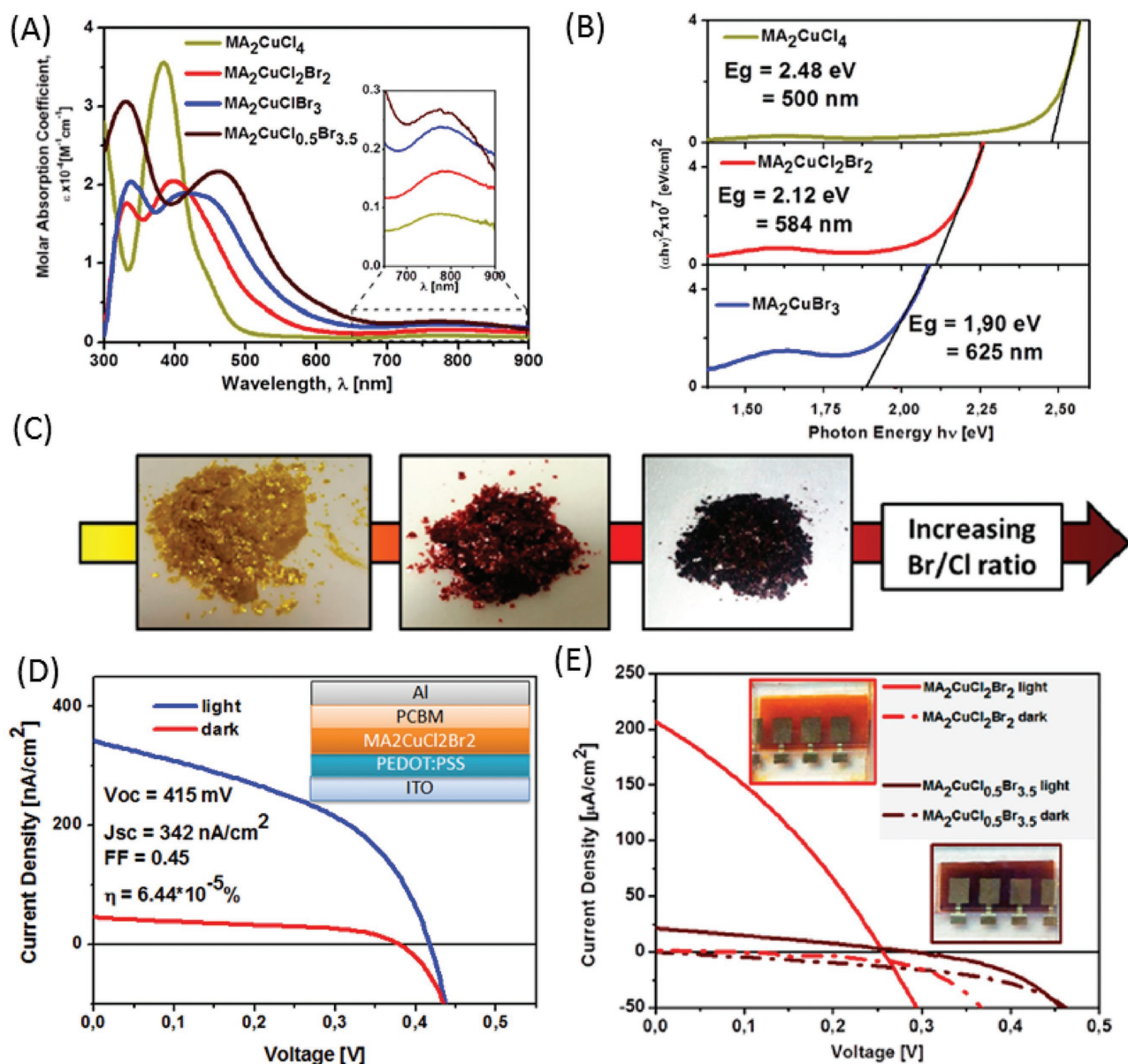


Figure 27. A) Absorption coefficient of $\text{MA}_2\text{CuCl}_x\text{Br}_{4-x}$. B) Tauc plots for MA_2CuCl_4 , $\text{MA}_2\text{CuCl}_2\text{Br}_2$ and MA_2CuBr_3 perovskite showing optical bandgaps of 2.48, 2.12, and 1.90 eV, respectively. C) Shift of $\text{MA}_2\text{CuCl}_x\text{Br}_{4-x}$ color with different Br/Cl ratio. D) J - V curve for $\text{MA}_2\text{CuCl}_2\text{Br}_2$ PSCs fabricated with planar heterojunction structure showing negligible photoelectronic performance. E) J - V curves for $\text{MA}_2\text{CuCl}_2\text{Br}_2$ and $\text{MA}_2\text{CuCl}_{0.5}\text{Br}_{3.5}$ PSCs fabricated with TiO_2 -based mesoporous structure measured under simulated AM 1.5 light illumination (solid curves) and in the dark (dash curves) showing PCE of 0.017 and 0.0017% for $\text{MA}_2\text{CuCl}_2\text{Br}_2$ and $\text{MA}_2\text{CuCl}_{0.5}\text{Br}_{3.5}$, respectively. Reproduced with permission.^[158] Copyright 2016, American Chemical Society.

a long room-temperature fundamental PL lifetime of ≈ 660 ns and an indirect bandgap of 1.95 eV, which is very encouraging for photovoltaic applications. Actually, many combinations of metals in different oxidation states can be incorporated into the B/B' sublattices, both organic and inorganic cations can be incorporated into the A sites, and the halide can also be varied. 2D layered Cu-based perovskite $\text{MA}_2\text{CuCl}_x\text{Br}_{4-x}$ was also explored for the first time with bandgap tunable characteristics by changing the Br content. Although the device performance is still low due to a low absorption coefficient and heavy mass of holes, it lays the foundation for further development of a perovskite based on transition metals as alternative lead-free materials.

The emergence of lead-free perovskites as a new class of remarkable semiconductors has been intensively investigated for photovoltaic applications in the past few years. It can be further expanded into other technological areas such as lasers, detectors, transistors, and LEDs. The performance of lead-free PSCs; however, is now still far away from that of lead-based devices, as shown in **Table 1**. Although great effort has been made in lead-free perovskite photovoltaics (**Table 2**), our current knowledge of the lead-free perovskite materials is highly limited and needs to be further explored and challenged. Improved understanding of the fundamental photophysics could create new insights in controlling the optical, electronic, and

Table 1. Summary of device performance of lead-free perovskite solar cells.

Lead-free Perovskites	E_g [eV]	V_{oc} [V]	J_{sc} [mA cm^{-2}]	FF	PCE [%]	Ref.
CsSnI ₃	1.3	0.01	0.19	0.21	3×10^{-4}	[108]
CsSnI ₃ :CsSnBr ₃ (1:1)	1.5	0.135	3.69	0.26	0.13	[119]
CsSnI ₃ :SnF ₂	–	0.24	22.7	0.37	2.02	[108]
CsSn ₂ Br:SnF ₂	1.37	0.289	15.06	0.38	1.67	[119]
MASnI ₃	1.23	0.88	16.8	0.42	6.4	[87]
FASnI ₃ :SnF ₂	1.41	0.262	12.4	0.44	1.41	[111]
FASnI ₃ :pyrazine	–	0.29	24.5	0.55	4	[106]
CsGeI ₃	1.6	0.074	5.7	27	0.11	[122,123]
MAGeI ₃	1.9	0.15	4	30	0.2	[122,123]
Cs ₃ Bi ₂ I ₉	2.2	0.85	2.15	0.6	1.09	[136]
MA ₃ Bi ₂ I ₉	2.1	0.68	0.52	0.33	0.12	[136]
MA ₃ Bi ₂ I ₉ Cl _x	2.4	0.04	0.18	0.38	0.003	[136]
Cs ₃ Sb ₂ I ₉	2.05	0.25–0.3	–	–	<1	[143]
MA ₂ CuCl ₂ Br ₂	2.12	0.256	0.216	0.32	0.017	[158]
MA ₂ CuCu _{10.5} Br _{3.5}	1.8	0.29	0.021	0.28	0.002	[158]

charge-transport properties. An integrated theoretical calculation and modeling strategy could play a major role in further advancing lead-free perovskite materials design. Controlling the micro/nano structure of lead-free perovskite is also important by exploring new methods or combining the existing technologies, e.g., solvent engineering, moisture assisted growth, additives, and hot spin-coating, and further improving the film

Table 2. Summary of lead-free perovskite materials from calculation (#) and/or from experiment (*) without device characterization.

Perovskites	E_g [eV]	Ref.
Cs ₂ SnI ₆	1.6	[109]*
CsSnS ₂ Cl	1.1	[80]#
CsGeBr ₃	2.32	[123]*
CsGeCl ₃	3.67	[123]*
FOGeI ₃	2.2	[123]*
MFOGeI ₃	2.5	[123]*
Cs ₃ Bi ₂ I ₉	1.9	[154]*
Cs ₂ AgBiBr ₆	2.19	[152]*
Cs ₂ AgBiCl ₆	2.77	[154]*
MABiSCL ₂	2	[80]#
MABiSBr ₂	1.68	[80]#
MABiSI ₂	1.38	[80]#
MABiSeCl ₂	1.9	[80]#
MABiSeBr ₂	1.59	[80]#
MABiSeI ₂	1.29	[80]#
MABiTeCl ₂	1.58	[80]#
MABiTeBr ₂	1.44	[80]#
MABiTeI ₂	1.24	[80]#
MA ₃ Bi ₂ I ₉	1.94	[137]*
Cs ₃ Sb ₂ I ₉	2.05	[137]*

quality allows for an improved performance of lead-free perovskite devices. The energy match between the lead-free perovskite and the charge transporting layer cannot be ruled out since the energy levels of lead-free perovskites are significant different from lead perovskites and new charge transporting materials also need to be developed. Accordingly, a PCE over 10% can be expected. All in all, we are convinced that lead-free perovskite materials have a bright future for photovoltaics and other optoelectronics, and could lead to exciting and useful discoveries by deep understanding into the band structure and transport properties.

Acknowledgements

This work was financially supported by the National Basic Research Program of China-Fundamental Studies of Perovskite Solar Cells (2015CB932200), Natural Science Foundation of Jiangsu Province, China (55135039, 55135040), and Startup from Nanjing Tech University (3983500160, 3983500151, ZKRC201514).

Received: September 16, 2016
Revised: October 22, 2016
Published online:

- [1] A. Kojima, K. Teshima, Y. Shirai, T. Miyasaka, *J. Am. Chem. Soc.* **2009**, *131*, 6050.
- [2] M. M. Lee, J. Teuscher, T. Miyasaka, T. N. Murakami, H. J. Snaith, *Science* **2012**, *338*, 643.
- [3] S. D. Stranks, G. E. Eperon, G. Grancini, C. Menelaou, M. J. P. Alcocer, T. Leijtens, L. M. Herz, A. Petrozza, H. J. Snaith, *Science* **2013**, *342*, 341.
- [4] G. C. Xing, N. Mathews, S. Sun, S. S. Lim, Y. M. Lam, M. Grätzel, S. Mhaisalkar, T. C. Sum, *Science* **2013**, *342*, 344.
- [5] M. Sessolo, H. J. Bolink, *Science* **2015**, *350*, 917.
- [6] W. Chen, Y. Wu, Y. Yue, J. Liu, W. Zhang, X. Yang, H. Chen, E. Bi, I. Ashraf, M. Grätzel, L. Han, *Science* **2015**, *350*, 944.

- [7] P. Gao, M. Graetzel, M. K. Nazeeruddin, *Energ. Environ. Sci.* **2014**, *7*, 2448.
- [8] O. Malinkiewicz, A. Yella, Y. H. Lee, G. M. Espallargas, M. Graetzel, M. K. Nazeeruddin, H. J. Bolink, *Nat. Photonics* **2014**, *8*, 128.
- [9] J. Xu, A. Buin, A. H. Ip, W. Li, O. Voznyy, R. Comin, M. Yuan, S. Jeon, Z. Ning, J. J. McDowell, P. Kanjanaboos, J.-P. Sun, X. Lan, L. N. Quan, D. H. Kim, I. G. Hill, P. Maksymovych, E. H. Sargent, *Nat. Commun.* **2015**, *6*, 7081.
- [10] P. Docampo, J. M. Ball, M. Darwich, G. E. Eperon, H. J. Snaith, *Nat. Commun.* **2013**, *4*, 2761.
- [11] J. H. Heo, S. H. Im, J. H. Noh, T. N. Mandal, C.-S. Lim, J. A. Chang, Y. H. Lee, H.-J. Kim, A. Sarkar, M. K. Nazeeruddin, M. Grätzel, S. I. Seok, *Nat. Photonics* **2013**, *7*, 487.
- [12] J. N. Burschka, N. Pellet, S.-J. Moon, R. Humphry-Baker, P. Gao, M. K. Nazeeruddin, M. Grätzel, *Nature* **2013**, *499*, 316.
- [13] Z. Xiao, Q. Dong, C. Bi, Y. Shao, Y. Yuan, J. Huang, *Adv. Mater.* **2014**, *26*, 6503.
- [14] X. Li, D. Bi, C. Yi, J.-D. Décoppet, J. Luo, S. M. Zakeeruddin, A. Hagfeldt, M. Grätzel, *Science* **2016**, *353*, 6294.
- [15] Y. Chen, T. Chen, L. Dai, *Adv. Mater.* **2015**, *27*, 1053.
- [16] D. Y. Liu, T. L. Kelly, *Nat. Photonics* **2014**, *8*, 133.
- [17] D. P. McMeekin, G. Sadoughi, W. Rehman, G. E. Eperon, M. Saliba, M. T. Hörantner, A. Haghighirad, N. Sakai, L. Korte, B. Rech, M. B. Johnston, L. M. Herz, H. J. Snaith, *Science* **2016**, *351*, 151.
- [18] C. Bi, Q. Wang, Y. Shao, Y. Yuan, Z. Xiao, J. Huang, *Nat. Commun.* **2015**, *6*, 7747.
- [19] A. Mei, X. Li, L. Liu, Z. Ku, T. Liu, Y. Rong, M. Xu, M. Hu, J. Chen, Y. Yang, M. Grätzel, H. Han, *Science* **2014**, *345*, 295.
- [20] W. S. Yang, J. H. Noh, N. J. Jeon, Y. C. Kim, S. Ryu, J. Seo, S. I. Seok, *Science* **2015**, *348*, 1234.
- [21] D. Bi, W. Tress, M. I. Dar, P. Gao, J. Luo, C. m. Renevier, K. Schenk, A. Abate, F. Giordano, J. P. Correa Baena, J.-D. Decoppet, S. M. Zakeeruddin, M. K. Nazeeruddin, M. Grätzel, A. Hagfeldt, *Sci. Adv.* **2016**, *2*, e1501170.
- [22] NREL: National Center For Photovoltaics Home Page, www.nrel.gov/ncpv (accessed: September, 2016).
- [23] Y. Zhao, K. Zhu, *Chem. Soc. Rev.* **2016**, *45*, 655.
- [24] N. H. Tiep, Z. Ku, H. J. Fan, *Adv. Energy Mater.* **2016**, *6*, 1501420.
- [25] X. Lü, Y. Wang, C. C. Stoumpos, Q. Hu, X. Guo, H. Chen, L. Yang, J. S. Smith, W. Yang, Y. Zhao, H. Xu, M. G. Kanatzidis, Q. Jia, *Adv. Mater.* **2016**, *28*, 8663.
- [26] N. J. Jeon, J. H. Noh, W. S. Yang, Y. C. Kim, S. Ryu, J. Seo, S. I. Seok, *Nature* **2015**, *517*, 476.
- [27] J. Albero, A. M. Asiri, H. Garcia, *J. Mater. Chem. A* **2016**, *4*, 4353.
- [28] J. Chen, S. Zhou, S. Jin, H. Li, T. Zhai, *J. Mater. Chem. C* **2016**, *4*, 11.
- [29] D. Prochowicz, M. Franckevičius, A. M. Cieślak, S. M. Zakeeruddin, M. Grätzel, J. Lewiński, *J. Mater. Chem. A* **2015**, *3*, 20772.
- [30] P. C. Harikesh, H. K. Mulmudi, B. Ghosh, T. W. Goh, Y. T. Teng, K. Thirumal, M. Lockrey, K. Weber, T. M. Koh, S. Li, S. Mhaisalkar, N. Mathews, *Chem. Mater.* **2016**, *28*, 7496.
- [31] Y. Cheng, H. Li, J. Zhang, Q. Yang, T. Liu, Z. Guan, J. Qing, C. Lee, S. Tsang, *J. Mater. Chem. A* **2016**, *4*, 561.
- [32] G. E. Eperon, S. D. Stranks, C. Menelaou, M. B. Johnston, L. M. Herz, H. J. Snaith, *Energ. Environ. Sci.* **2014**, *7*, 982.
- [33] M. R. Leyden, M. V. Lee, S. R. Raga, Y. Qi, *J. Mater. Chem. A* **2015**, *3*, 16097.
- [34] G. E. Eperon, C. E. Beck, H. J. Snaith, *Mater. Horiz.* **2016**, *3*, 63.
- [35] N. Pellet, P. Gao, G. Gregori, T. Yang, M. K. Nazeeruddin, J. Maier, M. Grätzel, *Angew. Chem. Int. Ed.* **2014**, *53*, 3151.
- [36] D. E. Starr, G. Sadoughi, E. Handick, R. G. Wilks, J. H. Alsmeyer, L. Köhler, M. Gorgoi, H. J. Snaith, M. Bär, *Energy Environ. Sci.* **2015**, *8*, 1609.
- [37] L. Huang, Z. Hu, G. Yue, J. Liu, X. Cui, J. Zhang, Y. Zhu, *Phys. Chem. Chem. Phys.* **2015**, *17*, 22015.
- [38] T. M. Brenner, D. A. Egger, L. Kronik, G. Hodes, D. Cahen, *Nat. Rev. Mater.* **2016**, *1*, 15007.
- [39] J. H. Heo, S. H. Im, *Nanoscale* **2016**, *8*, 2554.
- [40] T. G. Kim, S. W. Seo, H. Kwon, J. Hahn, J. W. Kim, *Phys. Chem. Chem. Phys.* **2015**, *17*, 24342.
- [41] M. Jiang, J. Wu, F. Lan, Q. Tao, D. Gao, G. Li, *J. Mater. Chem. A* **2015**, *3*, 963.
- [42] J. Qing, H. Chandran, Y. Cheng, X. Liu, H. Li, S. Tsang, M. Lo, C. Lee, *ACS Appl. Mater. Inter.* **2015**, *7*, 23110.
- [43] W. Zhang, M. Saliba, D. T. Moore, S. K. Pathak, M. T. Hörantner, T. Stergiopoulos, S. D. Stranks, G. E. Eperon, J. A. Alexander-Webber, A. Abate, A. Sadhanala, S. Yao, Y. Chen, R. H. Friend, L. A. Estroff, U. Wiesner, H. J. Snaith, *Nat. Commun.* **2015**, *6*, 6142.
- [44] S. Dharani, H. A. Dewi, R. R. Prabhakar, T. Baikie, C. Shi, D. Yonghua, N. Mathews, P. P. Boix, S. G. Mhaisalkar, *Nanoscale* **2014**, *6*, 13854.
- [45] M. A. Green, A. Ho-Baillie, H. J. Snaith, *Nat. Photonics* **2014**, *8*, 506.
- [46] M. B. Johnston, L. M. Herz, *Accounts Chem. Res.* **2016**, *49*, 146.
- [47] N. Park, *Mater. Today* **2015**, *18*, 65.
- [48] Q. Shen, Y. Ogomi, J. Chang, T. Toyoda, K. Fujiwara, K. Yoshino, K. Sato, K. Yamazaki, M. Akimoto, Y. Kuga, K. Katayama, S. Hayase, *J. Mater. Chem. A* **2015**, *3*, 9308.
- [49] E. Koren, E. Lortscher, C. Rawlings, A. W. Knoll, U. Duerig, *Science* **2015**, *348*, 679.
- [50] D. Shi, V. Adinolfi, R. Comin, M. Yuan, E. Alarousu, A. Buin, Y. Chen, S. Hoogland, A. Rothenberger, K. Katsiev, Y. Losovyj, X. Zhang, P. A. Dowben, O. F. Mohammed, E. H. Sargent, O. M. Bakr, *Science* **2015**, *347*, 519.
- [51] C. Li, F. Wang, J. Xu, J. Yao, B. Zhang, C. Zhang, M. Xiao, S. Dai, Y. Li, Z. Tan, *Nanoscale* **2015**, *7*, 9771.
- [52] Y. Wang, H. Wang, M. Yu, L. Fu, Y. Qin, J. Zhang, X. Ai, *Phys. Chem. Chem. Phys.* **2015**, *17*, 29501.
- [53] J. Troughton, M. J. Carnie, M. L. Davies, C. Charbonneau, E. H. Jewell, D. A. Worsley, T. M. Watson, *J. Mater. Chem. A* **2016**, *4*, 3471.
- [54] S. M. Deetharaman, P. Nagarjuna, P. N. Kumar, S. P. Singh, M. Deepa, M. A. Namboothiry, *Phys. Chem. Chem. Phys.* **2014**, *16*, 24691.
- [55] H. Wang, Y. Wang, M. Yu, J. Han, Z. Guo, X. Ai, J. Zhang, Y. Qin, *Phys. Chem. Chem. Phys.* **2016**, *18*, 12128.
- [56] J. Zhao, P. Wang, L. Wei, Z. Liu, X. Fang, X. Liu, D. Ren, Y. Mai, *Dalton Trans* **2015**, *44*, 16914.
- [57] C. Bi, Y. Shao, Y. Yuan, Z. Xiao, C. Wang, Y. Gao, J. Huang, *J. Mater. Chem. A* **2014**, *2*, 18508.
- [58] B. Wang, K. Y. Wong, S. Yang, T. Chen, *J. Mater. Chem. A* **2016**, *4*, 3806.
- [59] B. Hailegnaw, S. Kirmayer, E. Edri, G. Hodes, D. Cahen, *J. Phys. Chem. Lett.* **2015**, *6*, 1543.
- [60] P. Patnaik, *Handbook of Inorganic Chemicals*; McGraw-Hill, New York **2003**.
- [61] K. Wang, Z. Liang, X. Wang, X. Cui, *Adv. Electron. Mater.* **2015**, *1*, 1500089.
- [62] G. Giorgi, J. Fujisawa, H. Segawa, K. Yamashita, *J. Phys. Chem. Lett.* **2013**, *4*, 4213.
- [63] J. Feng, B. Xiao, *J. Phys. Chem. Lett.* **2014**, *5*, 1278.
- [64] C. S. Wang, W. E. Pickett, *Phys. Rev. Lett.* **1983**, *51*, 597.
- [65] L. Hedin, *Phys. Rev.* **1965**, *139*, A796.
- [66] E. K. U. Gross, E. Runge, *Phys. Rev. Lett.* **1984**, *52*, 997.
- [67] A. D. Becke, *J. Chem. Phys.* **1993**, *98*, 5648.
- [68] W. Yang, R. G. Parr, C. Lee, *Phys. Rev. B* **1988**, *37*, 785.

- [69] J. P. Perdew, M. Ernzerhof, K. Burke, *J. Chem. Phys.* **1996**, *105*, 9982.
- [70] J. Heyd, G. E. Scuseria, M. Ernzerhof, *J. Chem. Phys.* **2003**, *118*, 8207.
- [71] A. V. Krkavau, O. A. Vydrov, A. F. Izmaylov, G. E. Scuseria, *J. Chem. Phys.* **2006**, *125*, 224106.
- [72] M. K. Y. Chan, G. Ceder, *Phys. Rev. Lett.* **2010**, *105*, 196403.
- [73] J. Harl, G. Kresse, *Phys. Rev. Lett.* **2009**, *103*, 56401.
- [74] J. Harl, L. Schimka, G. Kresse, *Phys. Rev. B* **2010**, *50*, 760.
- [75] M. Dion, H. Rydberg, E. Schroder, D. C. Langreth, B. I. Lundqvist, *Phys. Rev. Lett.* **2004**, *92*, 126402.
- [76] C. H. Li, X. G. Lu, W. Z. Ding, L. M. Feng, Y. H. Gao, Z. G. Guo, *Acta Crystallogr. B* **2008**, *64*, 702.
- [77] M. R. Filip, F. Giustino, *J. Phys. Chem. C* **2016**, *120*, 166.
- [78] P. Sun, Q. Li, L. Yang, Z. Li, *Nanoscale* **2016**, *8*, 1503.
- [79] K. Tanaka, T. Takahashi, T. Ban, T. Kondo, K. Uchida, N. Miura, *Solid State Commun.* **2003**, *127*, 619.
- [80] Y. Sun, J. Shi, J. Lian, W. Gao, M. L. Agiorgousis, P. Zhang, S. Zhang, *Nanoscale* **2016**, *8*, 6284.
- [81] W. Shockley, H. J. Queisser, *J. Appl. Phys.* **1961**, *32*, 510.
- [82] G. Giorgi, K. Yamashita, *Chem. Lett.* **2015**, *44*, 826.
- [83] F. Hong, B. Saparov, W. W. Meng, Z. W. Xiao, D. B. Mitzi, Y. F. Yan, *J. Phys. Chem. C* **2016**, *120*, 6435.
- [84] R. X. Yang, K. T. Butler, A. Walsh, *J. Phys. Chem. Lett.* **2015**, *6*, 5009.
- [85] C. C. Stoumpos, C. D. Malliakas, M. G. Kanatzidis, *Inorg. Chem.* **2013**, *52*, 9019.
- [86] P. Umari, E. Mosconi, F. De Angelis, *Sci. Rep.* **2014**, *4*, 4467.
- [87] N. K. Noel, S. D. Stranks, A. Abate, C. Wehrenfennig, S. Guarnera, A. Haghighirad, A. Sadhanala, G. E. Eperon, S. K. Pathak, M. B. Johnston, A. Petrozza, L. M. Herz, H. J. Snaith, *Energ. Environ. Sci.* **2014**, *7*, 3061.
- [88] F. Hao, C. C. Stoumpos, D. H. Cao, R. P. H. Chang, M. G. Kanatzidis, *Nat. Photonics* **2014**, *8*, 489.
- [89] J. H. Noh, S. H. Im, J. H. Heo, T. N. Mandal, S. I. Seok, *Nano Lett.* **2013**, *13*, 1764.
- [90] F. Hao, C. C. Stoumpos, R. P. H. Chang, M. G. Kanatzidis, *J. Am. Chem. Soc.* **2014**, *136*, 8094.
- [91] M. Z. Liu, M. B. Johnston, H. J. Snaith, *Nature* **2013**, *501*, 395.
- [92] Y. Zhao, K. Zhu, *J. Phys. Chem. C* **2014**, *118*, 9412.
- [93] J. Im, I. Jang, N. Pellet, M. Graetzel, N. Park, *Nat. Nanotechnol.* **2014**, *9*, 927.
- [94] H. Zhou, Q. Chen, G. Li, S. Luo, T. Song, H. Duan, Z. Hong, J. You, Y. Liu, Y. Yang, *Science* **2014**, *345*, 542.
- [95] G. E. Eperon, V. M. Burlakov, P. Docampo, A. Goriely, H. J. Snaith, *Adv. Funct. Mater.* **2014**, *24*, 151.
- [96] Y. Wu, A. Islam, X. Yang, C. Qin, J. Liu, K. Zhang, W. Peng, L. Han, *Energ. Environ. Sci.* **2014**, *7*, 2934.
- [97] M. Yang, T. Zhang, P. Schulz, Z. Li, G. Li, D. H. Kim, N. Guo, J. J. Berry, K. Zhu, Y. Zhao, *Nat. Comm.* **2016**, *7*, 12305.
- [98] N. J. Jeon, J. H. Noh, Y. C. Kim, W. S. Yang, S. Ryu, S. Il Seol, *Nat. Mater.* **2014**, *13*, 897.
- [99] F. Hao, C. C. Stoumpos, P. Guo, N. Zhou, T. J. Marks, R. P. H. Chang, M. G. Kanatzidis, *J. Am. Chem. Soc.* **2015**, *137*, 11445.
- [100] K. N. Liang, D. B. Mitzi, M. T. Prikas, *Chem. Mater.* **1998**, *10*, 403.
- [101] Q. Chen, H. Zhou, Z. Hong, S. Luo, H. Duan, H. Wang, Y. Liu, G. Li, Y. Yang, *J. Am. Chem. Soc.* **2014**, *136*, 622.
- [102] T. Yokoyama, D. H. Cao, C. C. Stoumpos, T. Song, Y. Sato, S. Aramaki, M. G. Kanatzidis, *J. Phys. Chem. Lett.* **2016**, *7*, 776.
- [103] U. Bansode, R. Naphade, O. Game, S. Agarkar, S. Ogale, *J. Phys. Chem. C* **2015**, *119*, 9177.
- [104] M. Weiss, J. Horn, C. Richter, D. Schlettwein, *Phys. Status Solidi A* **2016**, *213*, 975.
- [105] M. Jung, S. R. Raga, Y. Qi, *RSC Adv.* **2016**, *6*, 2819.
- [106] S. J. Lee, S. S. Shin, Y. C. Kim, D. Kim, T. K. Ahn, J. H. Noh, J. Seo, S. I. Seok, *J. Am. Chem. Soc.* **2016**, *138*, 3974.
- [107] I. Chung, J. H. Song, J. Im, J. Androulakis, C. D. Malliakas, H. Li, A. J. Freeman, J. T. Kenney, M. G. Kanatzidis, *J. Am. Chem. Soc.* **2012**, *134*, 8579.
- [108] M. H. Kumar, S. Dharani, W. L. Leong, P. P. Boix, R. R. Prabhakar, T. Baikie, C. Shi, H. Ding, R. Ramesh, M. Asta, M. Graetzel, S. G. Mhaisalkar, N. Mathews, *Adv. Mater.* **2014**, *26*, 7122.
- [109] B. Saparov, J. Sun, W. Meng, Z. Xiao, H. Duan, O. Gunawan, D. Shin, I. G. Hill, Y. Yan, D. B. Mitzi, *Chem. Mater.* **2016**, *28*, 2315.
- [110] I. Borriello, G. Cantele, D. Ninno, *Phys. Rev. B* **2008**, *77*, 223522.
- [111] T. M. Koh, T. Krishnamoorthy, N. Yantara, C. Shi, W. L. Leong, P. P. Boix, A. C. Grimsdale, S. G. Mhaisalkar, N. Mathews, *J. Mater. Chem. A* **2015**, *3*, 14996.
- [112] T. M. Koh, K. Fu, Y. Fang, S. Chen, T. C. Sum, N. Mathews, S. G. Mhaisalkar, P. P. Boix, T. Baikie, *J. Phys. Chem. C* **2014**, *118*, 16458.
- [113] D. Zhao, W. Q. Liao, Y. Yu, C. R. Grice, C. L. Wang, A. J. Cimaroli, P. Schulz, W. W. Meng, K. Zhu, R. G. Xiong, Y. F. Yan, *Adv. Mater.* **2016**, *28*, 9333.
- [114] Y. Y. Zhou, H. F. Garces, B. S. Senturk, A. L. Ortiz, N. P. Pature, *Mater. Lett.* **2013**, *110*, 127.
- [115] K. Shum, Z. Chen, J. Qureshi, C. L. Yu, J. J. Wang, W. Pfenninger, N. Vockic, J. Midgley, J. T. Kenney, *Appl. Phys. Lett.* **2010**, *96*, 221903.
- [116] S. Dharani, H. K. Mulmudi, N. Yantara, P. Trang, N. G. Park, M. Graetzel, S. Mhaisalkar, N. Mathews, P. P. Boix, *Nanoscale* **2014**, *6*, 1675.
- [117] Z. Chen, J. J. Wang, Y. Ren, C. Yu, K. Shum, *Appl. Phys. Lett.* **2012**, *101*, 93901.
- [118] K. P. Marshall, R. I. Walton, R. A. Hatton, *J. Mater. Chem. A* **2015**, *3*, 11631.
- [119] D. Sabba, H. K. Mulmudi, R. R. Prabhakar, T. Krishnamoorthy, T. Baikie, P. P. Boix, S. Mhaisalkar, N. Mathews, *J. Phys. Chem. C* **2015**, *119*, 1763.
- [120] Y. Zhou, N. Wang, M. Ju, H. F. Garces, T. Ding, S. Pang, X. C. Zeng, N. P. Pature, X. W. Sun, *Adv. Energy Mater.* **2016**, *6*, 1601130.
- [121] B. Lee, C. C. Stoumpos, N. Zhou, F. Hao, C. Malliakas, C. Yeh, T. J. Marks, M. G. Kanatzidis, R. P. H. Chang, *J. Am. Chem. Soc.* **2014**, *136*, 15379.
- [122] T. Krishnamoorthy, H. Ding, C. Yan, W. L. Leong, T. Baikie, Z. Zhang, M. Sherburne, S. Li, M. Asta, N. Mathews, S. G. Mhaisalkar, *J. Mater. Chem. A* **2015**, *3*, 23829.
- [123] C. C. Stoumpos, L. Frazer, D. J. Clark, Y. S. Kim, S. H. Rhim, A. J. Freeman, J. B. Ketterson, J. I. Jang, M. G. Kanatzidis, *J. Am. Chem. Soc.* **2015**, *137*, 6804.
- [124] T. Umebayashi, K. Asai, T. Kondo, A. Nakao, *Phys. Rev. B* **2003**, *67*, 155405.
- [125] M. H. Du, *J. Mater. Chem. A* **2014**, *2*, 9091.
- [126] R. D. Shannon, *Acta Crystallogr. A* **1976**, *32*, 751.
- [127] R. Mohan, *Nat. Chem.* **2010**, *2*, 336.
- [128] S. Abe, K. Masumoto, K. Suto, *J. Cryst. Growth* **1997**, *181*, 367.
- [129] A. Stavrinadis, A. K. Rath, F. P. G. de Arquer, S. L. Diedenhofen, C. Magén, L. Martinez, D. So, G. Konstantatos, *Nat. Commun.* **2013**, *4*, 2981.
- [130] N. Leblanc, N. Mercier, L. Zorina, S. Simonov, P. Auban-Senzier, C. Pasquier, *J. Am. Chem. Soc.* **2011**, *133*, 14924.
- [131] W. Bi, N. Leblanc, N. Mercier, P. Auban-Senzier, C. Pasquier, *Chem. Mater.* **2009**, *21*, 4099.
- [132] B. Chabot, E. Parthe, *Acta Crystallogr. B* **1978**, *34*, 645.
- [133] S. V. Melnikova, A. I. Zaitsev, *Phys. Solid State* **1997**, *39*, 1652.
- [134] Y. N. Ivanov, A. A. Sukhovskii, V. V. Lisin, I. P. Aleksandrova, *Inorg. Mater.* **2001**, *37*, 623.

- [135] P. Szklarz, A. Pietraszko, R. Jakubas, G. Bator, P. Z. Nski, M. Gałazka, *J. Phys-Condens. Mat.* **2008**, *20*, 5740.
- [136] B. Park, B. Philippe, X. Zhang, H. Rensmo, G. Boschloo, E. M. J. Johansson, *Adv. Mater.* **2015**, *27*, 6806.
- [137] K. Eckhardt, V. Bon, J. Getzschmann, J. Grothe, F. M. Wisser, S. Kaskel, *Chem. Commun.* **2016**, *52*, 3058.
- [138] M. Saba, M. Cadelano, D. Marongiu, F. Chen, V. Sarritzu, N. Sestu, C. Figus, M. Aresti, R. Piras, A. Geddo Lehmann, C. Cannas, A. Musinu, F. Quochi, A. Mura, G. Bongiovanni, *Nat. Commun.* **2014**, *5*, 5049.
- [139] V. D. Innocenzo, G. Grancini, M. J. P. Alcocer, A. R. S. Kandada, S. D. Stranks, M. M. Lee, G. Lanzani, H. J. Snaith, A. Petrozza, *Nat. Commun.* **2014**, *5*, 3586.
- [140] R. L. Z. Hoyer, R. E. Brandt, A. Osherov, V. Stevanović, S. D. Stranks, M. W. B. Wilson, H. Kim, A. J. Akey, J. D. Perkins, R. C. Kurchin, J. R. Poindexter, E. N. Wang, M. G. Bawendi, V. Bulović, T. Buonassisi, *Chem-Eur. J.* **2016**, *22*, 2605.
- [141] A. J. Lehner, D. H. Fabini, H. A. Evans, C. Hébert, S. R. Smock, J. Hu, H. Wang, J. W. Zwanziger, M. L. Chabiny, R. Seshadri, *Chem. Mater.* **2015**, *27*, 7137.
- [142] S. Sun, S. Tominaka, J. Lee, F. Xie, P. D. Bristowe, A. K. Cheetham, *Appl. Mater.* **2016**, *4*, 31101.
- [143] B. Saparov, F. Hong, J. Sun, H. Duan, W. Meng, S. Cameron, I. G. Hill, Y. Yan, D. B. Mitzi, *Chem. Mater.* **2015**, *27*, 5622.
- [144] Y. Kim, Z. Yang, A. Jain, O. Voznyy, G.-H. Kim, M. Liu, L. N. Quan, F. Pelayo, G. Arquer, R. Comin, J. Z. Fan, E. H. Sargent, *Angew. Chem. Int. Ed.* **2016**, *55*, 9586.
- [145] D. M. Fabian, S. Ardo, *J. Mater. Chem. A* **2016**, *4*, 6837.
- [146] D. B. Mitzi, P. Brock, *Inorg. Chem.* **2001**, *40*, 2096.
- [147] G. A. Mousdis, G. C. Papavassiliou, A. Terzis, C. P. Raptopoulou, *Z. Naturforsch. B* **1998**, *53*, 927.
- [148] S. Vasala, M. Karppinen, *Prog. Solid State Chem.* **2015**, *43*, 1.
- [149] N. Kojima, *B. Chem. Soc. Jpn.* **2000**, *73*, 1445.
- [150] M. Retuerto, T. Emge, J. Hadermann, P. W. Stephens, M. R. Li, Z. P. Yin, M. Croft, A. Ignatov, S. J. Zhang, Z. Yuan, C. Jin, J. W. Simonson, M. C. Aronson, A. Pan, D. N. Basov, G. Kotliar, M. Greenblatt, *Chem. Mater.* **2013**, *25*, 4071.
- [151] L. O. Brockway, J. Y. Beach, *J. Am. Chem. Soc.* **1938**, *60*, 1836.
- [152] A. H. Slavney, T. Hu, A. M. Lindenberg, H. I. Karunadasa, *J. Am. Chem. Soc.* **2016**, *138*, 2138.
- [153] M. R. Filip, S. Hillman, A. A. Haghighirad, H. J. Snaith, F. Giustino, *J. Phys. Chem. Lett.* **2016**, *7*, 2579.
- [154] E. T. McClure, M. R. Ball, W. Windl, P. M. Woodward, *Chem. Mater.* **2016**, *28*, 1348.
- [155] G. Volonakis, M. R. Filip, A. A. Haghighirad, N. Sakai, B. Wenger, H. J. Snaith, F. Giustino, *J. Phys. Chem. Lett.* **2016**, *7*, 1254.
- [156] M. R. Filip, C. Verdi, F. Giustino, *J. Phys. Chem. C* **2015**, *119*, 25209.
- [157] F. Wei, Z. Deng, S. Sun, F. Xie, G. Kieslich, D. M. Evans, M. A. Carpenter, P. D. Bristowe, A. K. Cheetham, *Mater. Horiz.* **2016**, *3*, 328.
- [158] D. Cortecchia, H. A. Dewi, J. Yin, A. Bruno, S. Chen, T. Baikie, P. P. Boix, M. Grätzel, S. Mhaisalkar, C. Soci, N. Mathews, *Inorg. Chem.* **2016**, *55*, 1044.